Simulating CH_4 and CO_2 over South and East Asia using the zoomed chemistry transport model LMDzINCA

Xin Lin[1], Philippe Ciais[1], Philippe Bousquet[1], Michel Ramonet[1], Yi Yin[1a], Yves Balkanski[1], Anne Cozic[1], Marc Delmotte[1], Nikolaos Evangeliou[2], Nuggehalli K. Indira[3], Robin Locatelli[1b], Shushi Peng[4], Shilong Piao[4], Marielle Saunois[1], Panangady S. Swathi[3], Rong Wang[1c], Camille Yver-Kwok[1], Yogesh K. Tiwari[5], Lingxi Zhou[6]

Affiliations:

[1]Laboratoire des Sciences du Climat et de l'Environnement, LSCE-IPSL (CEA-CNRS-UVSQ), Université Paris-Saclay, 91191 Gif-sur-Yvette, France

[2]Norwegian Institute for Air Research (NILU), Department of Atmospheric and Climate Research (ATMOS), Kjeller, Norway

[3]CSIR Fourth Paradigm Institute (formerly CSIR Centre for Mathematical Modelling and Computer Simulation), NAL Belur Campus, Bengaluru 560 037, India

[4]Sino-French Institute for Earth System Science, College of Urban and Environmental Sciences, Peking University, Beijing 100871, China

[5]Centre for Climate Change Research, Indian Institute of Tropical Meteorology, Pune, India

[6]Chinese Academy of Meteorological Sciences (CAMS), China Meteorological Administration (CMA), Beijing, China

Correspondence to: X. Lin (xin.lin@lsce.ipsl.fr)

[a]Now at: California Institute of Technology, Pasadena, CA, USA
[b]Now at: AXA Global P&C, Paris, France
[c]Now at: Department of Environmental Science and Engineering, Fudan University, Shanghai 200433, China

Abstract

The increasing availability of atmospheric measurements of greenhouse gases (GHGs) from surface stations can improve the retrieval of their fluxes at higher spatial and temporal resolutions by inversions, provided that transport models are able to properly represent the variability of concentrations observed at different stations. South and East Asia (SEA) is a region with large and very uncertain emissions of carbon dioxide (CO_2) and methane (CH_4), the most potent anthropogenic GHGs. Monitoring networks have expanded greatly during the past decade in this region, which should contribute to reducing uncertainties in estimates of regional GHG budgets. In this study, we simulate concentrations of CH_4 and CO_2 using zoomed versions (abbreviated as 'ZAs') of the global chemistry transport model LMDzINCA, which have fine horizontal resolutions of ~0.66° in longitude and ~0.51° in latitude over SEA and coarser resolutions elsewhere. The concentrations of CH_4 and CO_2 simulated from ZAs are compared to those from the same model but with standard model grids of 2.50° in longitude and 1.27° in latitude (abbreviated as 'STs'), both prescribed with the same natural and anthropogenic fluxes. Model performance is evaluated for each model version at multi-annual, seasonal, synoptic and diurnal scales, against a unique observation dataset including 39 global and regional stations over SEA and around the world. Results show that ZAs improve the overall representation of CH_4 annual gradients between stations in SEA, with reduction of RMSE by 16–20% compared to STs. The model improvement mainly results from reduction in representation error at finer horizontal resolutions and thus better characterization of the CH_4 concentration gradients related to scatterly distributed emission sources. However, the performance of ZAs at a specific station as compared to STs is more sensitive to errors in meteorological forcings and surface fluxes, especially when short-term variabilities or stations close to source regions are examined. This highlights importance of accurate a priori CH_4 surface fluxes in high resolution transport modelling and inverse studies, particularly regarding locations and magnitudes of emission hotspots. Model performance for CO_2 suggests that the CO_2 surface fluxes have not been prescribed with sufficient accuracy and resolution, especially the spatio-temporally varying carbon exchange between land surface and atmosphere. Besides, representation of the CH_4 and CO_2 short-term variabilities is also limited by model's ability to simulate boundary layer mixing and mesoscale transport in complex terrains, emphasizing the need to improve sub-grid physical parameterizations in addition to refinement of model resolutions.

1 Introduction

Despite attrition in the global network of greenhouse gas (GHG) monitoring stations (Houweling et al., 2012), new surface stations have been installed since the late 2000s in the northern industrialized continents such as Europe (e.g., Aalto et al., 2007; Lopez et al., 2015; Popa et al., 2010), North America (e.g., Miles et al., 2012), and Northeast Asia (e.g., Fang et al., 2014; Sasakawa et al., 2010; Wada et al., 2011; Winderlich et al., 2010). In particular, the number of continuous monitoring stations over land has increased (e.g., Aalto et al., 2007; Lopez et al., 2015; Winderlich et al., 2010) given that more stable and precise instruments are available (e.g., Yver Kwok et al., 2015). These observations can be assimilated in inversion frameworks that combine them with a chemistry transport model and prior knowledge of fluxes to optimize GHG sources and sinks (e.g., Berchet et al., 2015; Bergamaschi et al., 2010, 2015, Bousquet et al., 2000, 2006; Bruhwiler et al., 2014; Gurney et al., 2002; Peters et al., 2010; Rödenbeck et al., 2003). Given the increasing observation availability, GHG budgets are expected to be retrieved at finer spatial and temporal resolutions by atmospheric inversions if the atmospheric GHG variability can be properly modeled at theses scales. A first step of any source optimization is to evaluate the ability of chemistry transport models to represent the variabilities of GHG concentrations, as transport errors are recognized as one of the main uncertainties in atmospheric inversions (Locatelli et al., 2013).

Many previous studies have investigated regional and local variations of atmospheric GHG concentrations using atmospheric chemistry transport models, with spatial resolutions ranging 100–300 km for global models (e.g., Chen and Prinn, 2005; Feng et al., 2011; Law et al., 1996; Patra et al., 2009a, 2009b) and 10–100 km for regional models (e.g., Aalto et al., 2006; Chevillard et al., 2002; Geels et al., 2004; Wang et al., 2007). Model intercomparison experiments showed that the atmospheric transport models with higher horizontal resolutions are more capable of capturing the observed short-term variability at continental sites (Geels et al., 2007; Law et al., 2008; Maksyutov et al., 2008; Patra et al., 2008; Saeki et al., 2013), due to reduction of representation errors (point measured versus gridbox-averaged modeled concentrations), improved model transport, and more detailed description of surface fluxes and topography (Patra et al., 2008). However, a higher horizontal model resolution also demands high-quality meteorological forcings and prescribed surface fluxes as boundary conditions (Locatelli et al., 2015a).

Two main approaches have been deployed, in an Eulerian modeling context, to address the need for high-resolution transport modeling of long-lived GHGs. The first approach is to define a high-resolution grid mesh in a limited spatial domain of interest, and to nest it within a global model with varying degrees of sophistication to get boundary conditions for the GHGs advected inside/outside the regional domain (Bergamaschi et al., 2005, 2010; Krol et al., 2005; Peters et al., 2004). The second approach is to stretch the grid of a global model over a specific region (the so-called 'zooming') while maintaining all parameterizations consistent (Hourdin et al., 2006). For the former approach, several nested high-resolution zooms can be embedded into the same model (Krol et al., 2005) to focus on different regions. The 'zooming' approach has the advantage to avoid the nesting problems (e.g., tracer discontinuity, transport parameterization inconsistency) at the boundaries between a global and a regional model. In this study, we use the zooming capability of the LMDz model (Hourdin et al., 2006).

South and East Asia (hereafter 'SEA') has been the largest anthropogenic GHG emitting region since the mid 2000s due to its rapid socioeconomic development (Boden et al., 2015; Olivier et al., 2015; Le Quéré et al., 2015; Tian et al., 2016). Compared to Europe and North America where sources and sinks of GHGs are partly constrained by atmospheric observational networks, the quantification of regional GHG fluxes over SEA from atmospheric inversions remains uncertain due to the low density of surface observations (e.g., Patra et al., 2013; Swathi et al., 2013; Thompson et al., 2014, 2016). During the past decade, a number of new surface stations have been deployed (e.g., Fang et al., 2016, 2014; Ganesan et al., 2013; Lin et al., 2015; Tiwari and Kumar, 2012), which have the potential to provide new and useful constraints on estimates of GHG fluxes in this region. However, modeling GHG concentrations at these stations is challenging since they are often located in complex terrains (e.g. coasts or mountains) or close to large local sources of multiple origins. To fully take advantage of the new surface observations in SEA, forward modeling studies based on high-resolution transport models are needed to evaluate the ability of the inversion framework to assimilate such new observations.

In this study, we apply the chemistry transport model LMDzINCA (Folberth et al., 2006; Hauglustaine et al., 2004; Hourdin et al., 2006; Szopa et al., 2013) zoomed to a horizontal resolution of ~50km over SEA to simulate the variations of CH_4 and CO_2 during the period 2006–2013. The model performance is evaluated against observations from 39 global and

regional stations inside and outside the zoomed region. The variability of the observed or simulated concentrations at each station is decomposed for evaluation at different temporal scales, namely: the annual mean gradients between stations, the seasonal cycle, the synoptic variability and the diurnal cycle. For comparison, a non-zoomed standard version of the same transport model is also run with the same set of surface fluxes to estimate the improvement gained from the zoomed configuration. The detailed description of the observations and the chemistry transport model is presented in Section 2, together with the prescribed CH_4 and CO_2 surface fluxes that force the simulations, and the metrics used to quantify the model performance. The evaluation of the simulations performed is presented and discussed in Section 3, showing capabilities of the transport model to represent the annual gradients between stations, and the seasonal, synoptic, and diurnal variations. Conclusions and implications drawn from this study are given in Section 4.

2 Data and Methods

2.1 Model description

2.1.1 LMDzINCA

The LMDzINCA model couples a general circulation model developed at the Laboratoire de Météorologie Dynamique (LMD; Hourdin et al., 2006), and a global chemistry and aerosol model INteractions between Chemistry and Aerosols (INCA; Folberth et al., 2006; Hauglustaine et al., 2004). A more recent description of LMDzINCA is presented in Szopa et al. (2013). To simulate CH_4 and CO_2 concentrations, we run a standard version of the model with a horizontal resolution of 2.5° (i.e., 144 model grids) in longitude and 1.27° (i.e., 142 model grids) in latitude (hereafter this version is abbreviated as 'STs') and a zoomed version with the same number of grid boxes, but a resolution of ~0.66° in longitude and ~0.51° in latitude in a region of 50–130°E and 0–55°N centered over India and China (hereafter this version is abbreviated as 'ZAs') (Figure 1; see also Wang et al., 2014, 2016). It means that, in terms of the surface area, a gridcell from STs roughly contains 9 grid-cells from ZAs within the zoomed region. Both model versions are run with 19 and 39 sigma-pressure layers, thus rendering four combinations of horizontal and vertical resolutions (i.e., ST19, ZA19, ST39, ZA39). Vertical diffusion and deep convection are parameterized following the schemes of Louis (1979) and Tiedtke (1989), respectively. The simulated horizontal wind vectors (*u* and

v) are nudged towards the 6-hourly European Center for Medium Range Weather Forecast (ECMWF) reanalysis dataset (ERA-I) in order to simulate the observed large scale advection (Hourdin and Issartel, 2000).

The atmospheric concentrations of hydroxyl radicals (OH), the main sink of atmospheric CH_4, are produced from a simulation at a horizontal resolution of 3.75° in longitude (i.e., 96 model grids) and 1.9° in latitude (i.e., 95 model grids) with the full INCA tropospheric photochemistry scheme (Folberth et al., 2006; Hauglustaine et al., 2004, 2014). The OH fields are climatological monthly data, and are regridded to the standard and zoomed model grids, respectively. It should be noted that the spatiotemporal distributions of the OH concentrations have large uncertainties and vary greatly among different chemical transport models, therefore the choice of the OH fields may affect the evaluation for CH_4 (especially in terms of the annual gradients between stations and the seasonal cycles). In this study, as we focus more on the improvement of performance gained from refinement of the model resolution rather than model-observation misfits and model bias in CH_4 growth rates, the influences of OH variations on model improvement are assumed to be very small given that the OH fields for both ZAs and STs are regridded from a lower model resolution and thus don't show much difference between the two model versions.

The CH_4 and CO_2 concentrations are simulated over the period 2000–2013 with both STs and ZAs. The first six years (2000–2005) of the simulations are considered as model spin-up, thus we only compare the simulated CH_4 and CO_2 concentrations with observations during 2006–2013. The initial CH_4 concentration field is defined based on the optimized initial state from a CH_4 inversion that assimilates observations from 50+ global background stations over the period 2006–2012 (Locatelli, 2014; Locatelli et al., 2015b). The optimized initial CH_4 concentration field for the year 2006 is rescaled to the levels of the year 2000 and used as the initial state in our simulations. The time step of model outputs is hourly.

2.1.2 Prescribed CH_4 and CO_2 surface fluxes

The prescribed CH_4 and CO_2 surface fluxes used as model inputs are presented in Table 1. We simulate the CH_4 concentration fields using a combination of the following datasets: (1) the interannually varing anthropogenic emissions obtained from the Emission Database for Global Atmospheric Research (EDGAR) v4.2 FT2010 product (http://edgar.jrc.ec.europa.eu), including emissions from rice cultivation with the seasonal variations based on Matthews et

al. (1991) imposed to the original yearly data; (2) climatogical wetland emissions based on the scheme developed by Kaplan et al. (2006); (3) interannually and seasonally varying biomass burning emissions from Global Fire Emissions Database (GFED) v4.1 product (Randerson et al., 2012; Van Der Werf et al., 2017; http://www.globalfiredata.org/), (4) climatological termite emissions (Sanderson, 1996), (5) climatological ocean emissions (Lambert and Schmidt, 1993), and (6) climatological soil uptake (Ridgwell et al., 1999). Note that for anthropogenic emissions from sectors other than rice cultivation, the seasonal variations are much smaller, and monthly sector-specific dataset is currently not available for the whole study period. Therefore we do not consider seasonal variations in CH_4 emissions from those sectors. Based on these emission fields, the global CH_4 emissions in 2010 are 543 $TgCH_4$/yr, and 191 $TgCH_4$/yr over the zoomed region. For the years over which CH_4 anthropogenic emissions (namely, the years 2011–2013) were not available from the data sources when the simulations were performed, we use emissions for the year 2010.

The prescribed CO_2 fluxes used to simulate the concentration fields are based on the following datasets: (1) three variants (hourly, daily, and monthly means) of interannually varying fossil fuel emissions produced by the Institut für Energiewirtschaft und Rationelle Energieanwendung (IER), Universität Stuttgart on the basis of EDGARv4.2 product (hereafter IER-EDGAR, http://carbones.ier.uni-stuttgart.de/wms/index.html) (Pregger et al., 2007); (2) interannually and seasonally varying biomass burning emission from GFEDv4.1 (Randerson et al., 2012; Van Der Werf et al., 2017; http://www.globalfiredata.org/); (3) interannually and hourly varying terrestrial biospheric fluxes produced from outputs of the Organizing Carbon and Hydrology in Dynamic EcosystEm (ORCHIDEE) model; and (4) interannually and seasonally varying air-sea CO_2 gas exchange maps developed by NOAA's Pacific Marine Environmental Laboratory (PMEL) and Atlantic Oceanographic and Meteorological Laboratory (AOML) groups (Park et al., 2010). Here ORCHIDEE runs with the trunk version r1882 (source code available at https://forge.ipsl.jussieu.fr/orchidee/browser/trunk#ORCHIDEE with the revision number of r1882), using the same simulation protocol as the SG3 simulation in MsTMIP project (Huntzinger et al., 2013). The climate forcing data are obtained from CRUNCEP v5.3.2, while the yearly land use maps, soil map and other forcing data (e.g., monthly CO_2 concentrations) are as described in Wei et al. (2014). The sum of global net CO_2 surface fluxes in 2010 are 6.9 PgC/yr, and 3.9 PgC/yr over the zoomed region. For the CO_2 fossil fuel

emissions, the IER-EDGAR product is only available until 2009. To generate the emission maps for the years 2010–2013, we scaled the emission spatial distribution in 2009 using the global totals for these years based on the EDGARv4.2FT2010 datasets. The detailed information for each surface flux is listed in Table 1.

2.2 Atmospheric CH_4 and CO_2 observations

The simulated CH_4 and CO_2 concentrations are evaluated against observations from 39 global and regional stations within and outside the zoomed region, operated by different programs and organizations (Figure 1; Table 2). The stations where flask observations are published (25 stations in total) mainly belong to the cooperative program organized by the NOAA Earth System Research Laboratory (NOAA/ESRL, available at ftp://aftp.cmdl.noaa.gov/data/trace_gases/). We also use flask obervations from stations operated by China Meterological Administration (CMA, China) (the JIN, LIN and LON stations, see also Fang et al., 2014), Commonwealth Scientific and Research Organization (CSIRO, Australia) (the CRI station, Bhattacharya et al., 2009, available at http://ds.data.jma.go.jp/gmd/wdcgg/), Indian Institute of Tropical Meteorology (IITM, India) (the SNG station, see also Tiwari et al., 2014), and stations from the Indo-French cooperative research program (the HLE, PON and PBL stations, Lin et al., 2015; Swathi et al., 2013). All the CH_4 (CO_2) flask measurements are reported on or linked to the NOAA2004 (WMOX2007) calibration scale, which guarantees comparability between stations in terms of annual means.

The continuous CH_4 and CO_2 measurements are obtained from 13 stations operated by Korea Meteorological Administration (KMA, Korea) (the AMY and GSN stations), Aichi Air Environment Division (AAED, Japan) (the MKW station), Japan Meteorological Agency (JMA) (the MNM, RYO and YON stations), National Institute for Environmental Studies (NIES, Japan) (the COI and HAT stations), Agency for Meteorology, Climatology and Geophysics (BMKG, Indonesia) and Swiss Federal Laboratoires for Materials Testing and Research (Empa, Switzerland) (the BKT station). These datasets are available from the World Data Center for Greenhouse Gases (WDCGG, http://ds.data.jma.go.jp/gmd/wdcgg/). Besides, continuous CH_4 and CO_2 measurements are also available from HLE and PON that have been maintained by the Indo-French cooperative research program between LSCE in France and IIA and CSIR4PI in India (Table 2). All the continuous CH_4 (CO_2) measurements used in this

study are reported on or traceable to the NOAA2004 (WMOX2007) scale except AMY, COI and HAT. The CO_2 continuous measurements at COI are reported on the NIES95 scale, which is 0.10 to 0.14 ppm lower than WMO in a range between 355 and 385 ppm (Machida et al., 2009). The CH_4 continuous measurements at COI and HAT are reported on the NIES scale, with a conversion factor to WMO scale of 0.9973 (JMA and WMO, 2014). For AMY, the CH_4 measurements over most of the study period are reported on the KRISS scale but they are not traceable to the WMO scale (JMA and WMO, 2014); therefore, we discarded this station from the analyses of the CH_4 annual gradients between stations. The stations used in this study span a large range of geographic locations (marine, coastal, mountain or continental) with polluted or non-polluted environments. Both flask and continuous measurements are used to evaluate the model's ability in representing the annual gradient between stations, the seasonal cycle and the synoptic variability for CH_4 and CO_2. The continuous measurements are also used to analyze the diurnal cycle for these two gases.

To evaluate the model performance with regards to vertical transport, we also use observations of the CO_2 vertical profiles from passenger aircraft from the Comprehensive Observation Network for TRace gases by AIrLiner (CONTRAIL) project (Machida et al., 2008, http://www.cger.nies.go.jp/contrail/index.html). This dataset provides high-frequency CO_2 measurements made by on-board continuous CO_2 measuring equipments (CMEs) during commercial airflights between Japan and other Asian countries. The CONTRAIL data are reported on the NIES95 scale, which is 0.10 to 0.14 ppm lower than WMO in a range between 355 and 385 ppm (Machida et al., 2009). In this study, we select from the CONTRAIL dataset all the CO_2 vertical profiles over SEA during the ascending and descending flights for the period 2006–2011, which provided 1808 vertical profiles over a total of 32 airports (Figure S1 and S2).

2.3 Sampling methods and data processing

The model outputs are sampled at the nearest gridpoint and vertical level to each station for both STs and ZAs. For flask stations, the model outputs are extracted at the exact hour when each flask sample was taken. For continuous stations below 1000 m.a.s.l., since both STs and ZAs cannot reproduce accurately the nighttime CH_4 and CO_2 accumulation near the ground as in most transport models (Geels et al., 2007), only afternoon (12:00–15:00 LST) data are retained for further analyses of the annual gradients, the seasonal cycle and the synoptic

279 variability. For continuous stations above 1000 m.a.s.l., only nighttime (00:00–3:00 LST)
280 data are retained to avoid sampling local air masses advected by upslope winds from nearby
281 valleys. During daytime, the local valley ascendances and the complex terrain mesoscale
282 circulations cannot be captured by a global transport model.

283 The curve-fitting routine (CCGvu) developed by NOAA Climate Monitoring and Diagnostic
284 Laboratory (NOAA/CMDL) is applied to the modelled and observed CH_4 and CO_2 time
285 series to extract the annual means, monthly smoothed seasonal cycles and synoptic variations
286 (Thoning et al., 1989). For each station, a smoothed function is fitted to the observed or
287 modelled time series, which consists of a first-order polynomial for the growth rate, two
288 harmonics for the annual cycle (Levin et al., 2002; Ramonet et al., 2002), and a low-pass
289 filter with 80 and 667 days as short-term and long-term cutoff values, respectively (Bakwin et
290 al., 1998). The annual means and the mean seasonal cycle are calculated from the smoothed
291 curve and harmonics, while the synoptic variations are defined as the residuals between the
292 original data and the smoothed fitting curve. Note that we have excluded the observations
293 lying beyond three standard deviations of the residuals around the fitting curve, which are
294 likely to be outliers that are influenced by local fluxes. More detailed descriptions about the
295 curve-fitting procedures and the set-up of parameters can be found in Section 2.3 of Lin et al.
296 (2015).

297 For the CO_2 vertical profiles from the CONTRAIL passenger aircraft programme, since CO_2
298 data have been continuously taken every 10 seconds by the onboard CMEs, we average the
299 observed and corresponding simulated CO_2 time series into altitude bins of 1km from the
300 surface to the upper troposphere. We also divide the whole study area into four major
301 subregions for which we group all available CONTRAIL CO_2 profiles (Figure S1), namely
302 East Asia (EAS), the Indian sub-continent (IND), Northern Southeast Asia (NSA) and
303 Southern Southeast Asia (SSA). Given that there are model-observation discrepancies in CO_2
304 growth rates as well as misfits of absolute CO_2 concentrations, the observed and simulated
305 CONTRAIL time series have been detrended before comparisons of the vertical gradients. To
306 this end, over each subregion, we detrend for each altitude bin the observed and simulated
307 CO_2 time series, by applying the respective linear trend fit to the observed and simulated CO_2
308 time series of the altitude bin 3–4 km. This altitude bin is thus chosen as reference due to
309 greater data availability compared to other altitudes, and because this level is outside the
310 boundary layer where aircraft CO_2 data are more variable and influenced by local sources

(e.g. airports and nearby cities). The detrended CO_2 (denoted as ΔCO_2) referenced to the 3-4 km altitude are seasonally averaged for each altitude bin and each subregion, and the resulting vertical profiles of ΔCO_2 are compared between simulations and observations.

2.4 Metrics

In order to evaluate the model performance to represent observations at different time scales (annual, seasonal, synoptic, diurnal), following Cadule et al. (2010), we define a series of metrics and corresponding statistics for each time scale. All the metrics, defined below, are calculated for both observed and simulated CH_4 (CO_2) time series between 2006 and 2013.

2.4.1 Annual gradients between stations

As inversions use gradients to optimize surface fluxes, it is important to have a metric based upon cross-site gradients. We take Hanle in India (HLE – 78.96°N, 32.78°E, 4517 m a.s.l., Figure 1, Table 2) as a reference and calculate the mean annual gradients by subtracting CH_4 (CO_2) at HLE from those of other stations. HLE is a remote station in the free troposphere within SEA and is located far from any important source/sink areas for both CH_4 and CO_2. These characteristics make HLE an appropriate reference to calculate the gradients between stations. Concentration gradients to HLE are calculated for both observations and model simulations using the corresponding smoothed curves fitted with the CCGvu routine (see Section 2.3). The ability of ZAs and STs to represent the observed CH_4 (CO_2) annual gradients across all the available stations is quantified by the mean bias (MB, Eq. 1) and the root-mean-square deviation (RMSE, Eq. 2). In Eq. 1 and Eq. 2, m_i and o_i indicate respectively the modelled and observed CH_4 (CO_2) mean annual gradient relative to HLE for a station i.

$$MB = \frac{\sum_{i=1}^{N}(m_i - o_i)}{N} \quad (1)$$

$$RMSE = \sqrt{\frac{\sum_{i=1}^{N}(m_i - o_i)^2}{N}} \quad (2)$$

335 2.4.2 Seasonal cycle

336 Two metrics of the model ability to reproduce the observed CH_4 (CO_2) seasonal cycle are
337 considered, the phase and the amplitude. For each station, the seasonal phase is evaluated by
338 the Pearson correlation between the observed and simulated harmonics extracted from the
339 original time series, whereas the seasonal cycle amplitude is evaluated by the ratio of the
340 modelled to the observed seasonal peak-to-peak amplitudes based on the harmonics (A_m/A_o).

341 2.4.3 Synoptic variability

342 For each station, the performance of ZAs and STs to represent the phase (timing) of the
343 synoptic variability is evaluated by the Pearson correlation coefficient between the modelled
344 and observed synoptic deviations (residuals) around the corresponding smoothed fitting curve
345 (see Section 2.3), whereas the performance for the amplitude of the synoptic variability is
346 quantified by the ratio of standard deviations of the residual concentration variability between
347 the model and observations (i.e., Normalized Standard Deviation, NSD, Eq. 3). Further, the
348 overall ability of a model to represent the synoptic variability of CH_4 (CO_2) at a station is
349 quantified by the RMSE (Eq. 4), a metric that can be represented with the Pearson correlation
350 and the NSD in a Taylor diagram (Taylor, 2001). In Eq. 3 and Eq. 4, m_j (o_j) indicates the
351 modelled (observed) synoptic event j, whereas $\overline{m}$ ($\bar{o}$) indicates the arithmetic mean of all the
352 modelled (observed) synoptic events over the study period. Note that for the flask
353 measurements, j corresponds to the time when a flask sample was taken, whereas for the
354 continuous measurements, j corresponds to the early morning (00:00–03:00LST, for
355 mountain stations) or afternoon (12:00–15:00LST, for coastal or island stations) period of
356 each sampling day.

357 $$NSD = \frac{\sqrt{\frac{\sum_{j=1}^{N}(m_j-\overline{m})^2}{N}}}{\sqrt{\frac{\sum_{j=1}^{N}(o_j-\bar{o})^2}{N}}} \quad (3)$$

358 $$RMSE = \sqrt{\frac{\sum_{j=1}^{N}(m_j-o_j)^2}{N}} \quad (4)$$

2.4.4 Diurnal cycle

For each station, the model's ability to reproduce the mean CH_4 (CO_2) diurnal cycle phase in a month is evaluated by the correlation of the hourly mean composite modelled and observed values, whereas model performance on the diurnal cycle amplitude is evaluated by the ratio of the modelled to the observed peak-to-peak amplitudes ($^{A_m}/_{A_o}$). For each station, daily means are subtracted from the raw data to remove any influence of interannual, seasonal or even synoptic variations.

3 Results and discussions

3.1 Annual gradients

3.1.1 CH_4 annual gradients

The annual mean gradient between a station and the HLE reference station relates to the time integral of transport of sources/sinks within the regional footprint area of the station on top of the background gradient caused by remote sources. For CH_4, Figure 2a,b shows the scatterplot of the simulated and observed mean annual gradients to HLE for all stations. In general, all the four model versions capture the observed CH_4 gradients with reference to HLE, and the simulated gradients roughly distribute around the identity line (Figure 2a,b). Compared to stardard versions (STs), the zoom versions (ZAs) better represent the CH_4 gradients for stations within the zoomed region (closed circles in Figure 2a,b), with RMSE decreasing by 20% and 16% for 19- and 39-layer models (Figure 2a,b and Table S1a). Note that increasing vertical resolution does not much impact the overall model performance, but the combination with the zoomed grid (i.e. ZA39) may inflate the model-observation misfits at a few stations with strong sources nearby (e.g. TAP and UUM in Table S2a). The better performance of ZAs within the zoomed region is also found for different seasons (Figure S3). Outside the zoomed region (open circles in Figure 2a,b), the performance of ZAs does not significantly deteriorate despite the coarser resolution.

When looking into the model performance for different station types, ZAs generally better capture the gradients at coastal and continental stations within the zoomed region, given the substantial reduction of RMSE compared to STs (Table S1). For example, significant model

improvement is found at Shangdianzi (SDZ – 117.12°E, 40.65°N, 293m a.s.l.) and Pondicherry (PON – 79.86°E, 12.01°N, 30m a.s.l.) (Figure 2a,b), each having an average bias reduction of 28.1 (73.0%) and 30.3 (94.7%) ppb respectively compared to STs for the 39-layer model (Table S2). This improvement mainly results from reduction in representation error with higher model horizontal resolutions in the zoomed region, through better description of surface fluxes and/or transport around the stations. Particularly, given the presence of large CH_4 emission hotspots within the zoomed region (Figure S4), ZAs makes the simulated CH_4 fields more heterogeneous around emission hotspots (e.g., North China in Figure S5), having the potential to better represent stations nearby on an annual basis if the surface fluxes are prescribed with sufficient accuracy.

However, finer resolutions may enhance model-data misfits due to inaccurate meteorological forcings and/or surface flux maps. For example, for the coastal station Tae-ahn Peninsula (TAP – 126.13°E, 36.73°N, 21m a.s.l.) with significant emission sources nearby (Figure S6), both ZAs and STs overestimate the observed CH_4 gradients by > +15 ppb, and ZA39 perform even worse than other versions (Table S2). The poor model performance at TAP suggests that the prescribed emission sources are probably overestimated within the station's footprint area (also see the marine station GSN, Figure S6), and higher model resolutions (whether in horizontal or in vertical) tend to inflate the model-observation misfits in this case. Besides, as stated in several previous studies (Geels et al., 2007; Law et al., 2008; Patra et al., 2008), for a station located in a complex terrain (e.g. coastal or mountain sites), the selection of an appropriate gridpoint and/or model level to represent an observation is challenging. In this study we sample the gridpoint and model level nearest to the location of the station, which may not be the best representation of data sampling selection strategy (e.g. marine sector at coastal stations or strong winds) and could contribute to the model-observation misfits.

3.1.2 CO_2 annual gradients

Both ZAs and STs can generally capture the CO_2 annual gradients between stations, although not as well as for CH_4 (Figure 2c,d). In contrast with CH_4, ZAs does not significantly improve representation of CO_2 gradients for stations within the zoomed region, with the mean bias and RMSE close to those of STs (Table S1b). At a few stations (e.g., TAP, Figure S8), ZAs even degrade model performance (Table S2b), possibly related to misrepresentation of

CO_2 sources in the prescribed surface fluxes and transport effects. Again increasing model vertical resolution does not much impact the overall model performance.

With finer horizontal resolution, the model improvement to represent the annual gradients is more apparent for CH_4 than for CO_2. One of the reasons may point towards the quality of CO_2 surface fluxes, especially natural ones. They are spatially more diffuse than those of CH_4, and temporally more variable in response to weather changes (Parazoo et al., 2008; Wang et al., 2007). Therefore, the regional variations of net ecosystem exchange (NEE) not captured by the terrestrial ecosystem model (e.g. ORCHIDEE in this paper) may explain the worse model performance on the CO_2 annual gradients compared to CH_4, and less apparent model improvement. Further, the spatial resolution of the prescribed surface flux may also account for the difference in model improvement between CO_2 and CH_4 (e.g. the spatial resolution of anthropogenic emissions is 1° for CO_2 and 0.1° for CH_4). Therefore, with current setup of surface fluxes (Table 1), ZAs is more likely to resolve the spatial heterogeneity of CH_4 fields, and its improvement over STs is more apparent than that for CO_2.

3.2 Seasonal cycles

3.2.1 CH_4 seasonal cycles

The model performance for the seasonal cycle depends on quality of seasonal surface fluxes, atmospheric transport, and chemistry (for CH_4 only). For CH_4, both ZAs and STs very well capture the seasonal phases at most stations within the zoomed region (Figure 3a), and model resolutions (in both horizontal and vertical) do not significantly impact the simulated timing of seasonal maximum and minimum. The seasonal phases at Plateau Assy (KZM – 77.87°E, 43.25°N, 2524m a.s.l.), Waliguan (WLG – 100.90°E, 36.28°N, 3890m a.s.l.) and Ulaan Uul (UUM – 111.10°E, 44.45°N, 1012m a.s.l.) are not well represented, probably related to unresolved seasonally varying sources around these stations. The sensitivity test simulations prescribed with wetland emissions from ORCHIDEE outputs show much better model-observation agreement in seasonal phases (Figure S9). For stations ouside the zoomed region, the performance of ZAs is not degraded despite the coarser horizontal resolutions (Figure S10).

With respect to the seasonal amplitude, the performance of STs and ZAs shows significant difference at stations influenced by large emission sources. For example, the seasonal

amplitudes of AMY and TAP are strongly overestimated by STs (A_m/A_o =2.99 and A_m/A_o =5.11 for the 39-layer model; Figure 3a), while ZAs substantially decrease the simulated amplitudes at these two stations with improved model-observation agreement (A_m/A_o =2.24 and A_m/A_o =2.80 for the 39-layer model; Figure 3a). However, at SDZ the seasonal amplitude is even more exaggerated by ZAs, especially when higher vertical resolution is applied (A_m/A_o =1.70 and A_m/A_o =2.03 for ST39 and ZA39; Figure 3a). The two contrasting cases suggest that increasing horizontal resolution does not necessarily better represent CH_4 seasonal cycle, and model improvement/degradation depends on other factors such as accuracy of the temporal and spatial variations of prescribed fluxes, OH fields and meteorological forcings. Besides, as it is found for annual CH_4 gradients, we note that the simulated seasonal amplitudes at stations in East Asia (AMY, TAP, GSN and SDZ) are consistently higher than the observed ones (Figure 3a), implying that the prescribed CH_4 emissions are probably overestimated in this region.

3.2.2 CO_2 seasonal cycles

The CO_2 seasonal cycle mainly represents the seasonal cycle of NEE from ORCHIDEE convoluted with atmospheric transport. Figure 3b illustrates that both ZAs and STs well capture the CO_2 seasonal phases at most stations, and a high correlation (Pearson correlation R>0.8) between the simulated and observed CO_2 harmonics is found for 14 out of 20 stations within the zoomed region. However, the simulated onset of CO_2 uptake in spring or timing of the seasonal minima tend to be earlier than observations. This shift in phase can be as large as >1 month for several stations (e.g. HLE, JIN and PON in Figure 3b), yet cannot be reduced by solely refining model resolutions. At BKT in western Indonesia, the shape of the CO_2 seasonality is not well captured (R=0.27 and R=0.30 for ST39 and ZA39; Figure 3b). Given that representation of the CH_4 seasonal phase at BKT is very good (R=0.97 for ST39 and ZA39; Figure 3a), the unsatisfactory model performance for CO_2 suggests inaccurate seasonal variations in the prescribed surface fluxes such as NEE and/or fire emissions. As for CH_4, the performance of ZAs is not degraded outside the zoomed region despite the coarser horizontal resolutions (Figure S11).

With respect to the CO_2 seasonal amplitude, 10 out of 20 stations within the zoomed region are underestimated by more than 20%, most of which are mountain and continental stations (Figure 3b). The underestimation of CO_2 seasonal amplitudes at these stations is probably due to the underestimated carbon uptake in northern mid-latitudes by ORCHIDEE, which is the case for most land surface models currently available (Peng et al., 2015). Another reason may be related to the misrepresentation of CO_2 seasonal rectifier effect (Denning et al., 1995), which means that the covariance between carbon exchange (through photosynthesis and respiration) and vertical mixing may not be well captured in our simulations even with finer model resolutions.

3.3 Synoptic variability

3.3.1 CH_4 synoptic variability

The day-to-day variability of CH_4 and CO_2 residuals are influenced by the regional distribution of fluxes and atmospheric transport at the synoptic scale. For CH_4, as shown in Figure 4a, both STs and ZAs fairly well capture the phases of synoptic variability at most stations within the zoomed region, with 15 out of 18 stations showing model-observation correlation $r>0.3$. Increasing horizontal resolution can more or less impact model performance, yet the direction of change is station-dependent. In general, ZAs improve correlation in phases for most marine and coastal stations compared to STs (e.g., CRI and HAT; Figure 4a), while degradation in model performance is mostly found for mountain and continental stations (e.g. KZM and SDZ; Figure 4a). With increased horizontal resolution, better characterization of the phases would require accurate representation of short-term variability in both meteorological forcings and emission sources at fine scales. This presents great challenges on data quality of boundary conditions, especially for mountain stations located in complex terrains or continental stations surrounded by highly heterogeneous yet uncertain emission sources.

Regarding the amplitudes of CH_4 synoptic variability, 12 out of 18 stations have NSDs within the range of 0.6–1.5, and ZAs generally give higher NSD values than STs for most of these stations (Figure 4b). For stations with NSDs>1.5, ZAs tend to simulate smaller amplitudes and slightly improve model performance (e.g., GSN, HLE and SDZ; Figure 4b). One exception is UUM. Given the presence of a wrong emission hotspot near the station in the EDGARv4.2FT2010 dataset (Figure S6), ZAs greatly inflate the model-observation misfits

(Figure S13). The sensitivity test simulations prescribed with an improved data version EDGARv4.3.2 show much better agreement with observations, although the simulated amplitudes are still too high (Figure S13). Besides, it is interesting to note that stations in East Asia generally have NSDs>1.5 (e.g., GSN, TAP, SDZ, and UUM; Figure 4b), again suggesting overestimation of the prescribed CH_4 emissions in this region.

3.3.2 CO_2 synoptic variability

For CO_2, as shown in Figure 4c and 4d, 12 out of 20 stations within the zoomed region have model-observation correlation r>0.3, whereas 14 out of 20 stations have NSDs within the range of 0.5–1.5. With finer model resolution, significant model improvement (whether regarding phases or amplitudes of CO_2 synoptic variability) is mostly found at marine, coastal and continental stations (e.g., AMY, DSI, and SDZ; Figure 4c,d); for mountain stations, on the contrary, phase correlation is not improved and representation of amplitudes is even degraded (e.g. HLE, LLN and WLG; Figure 4c,d). As mentioned above for CH_4 synoptic variablity, the model degradation at mountain stations may arise from errors in mesoscale meteorology and regional distribution of sources/sinks over complex terrains, probably as well as unresolved vertical processes.

When we examine model performance for CO_2 versus CH_4 by stations, there are stations at which phases of synoptic variability are satisfactorily captured for CH_4 but not for CO_2 (e.g., BKT, PBL, PON; Figure 4a,c). At PON, a tropical station on the southeast coast of India, the simulated CO_2 synoptic variability is even out of phase with observations all year around and during different seasons (Figure S14; Table S3). The poor model performance should be largely attributed to the imperfect prescribed CO_2 surface fluxes. As noted by several previous studies (e.g., Patra et al., 2008), CO_2 fluxes with sufficient accuracy and resolution are indispensable for realistic simulation of CO_2 synoptic variability. In this study, the daily to hourly NEE variability does not seem to be well represented in ORCHIDEE, especially in the tropics. Further, for stations influenced by large fire emissions (e.g., BKT), using the monthly averaged biomass burning emissions may not be able to realistically simulate CO_2 synoptic variability due to episodic biomass burning events. Besides, the prescribed CO_2 ocean fluxes have a rather coarse spatial resolution (4°×5°), which may additionally account for the poor model performance, especially for marine and coastal stations.

3.4 Diurnal cycle

3.4.1 CH_4 diurnal cycle

The diurnal cycles of trace gases are mainly controlled by the co-variations between local surface fluxes and atmospheric transport. To illustrate model performance on diurnal cycles, we take a few stations with continuous measurements as examples. For CH_4, as shown in Figure 5a, the mean diurnal cycles can be reasonably well represented at the marine/coastal stations GSN and PON for the specific study periods (also see Table S4), although monthly fluxes are used to prescribe the models. Compared to STs, the diurnal cycles simulated by ZAs agree much better with observations (Figure 5a), possibly due to more realistic representation of coastal topography, land-sea breeze, and/or source distribution at finer grids. However, there are also periods during which the CH_4 diurnal cycles are not satisfactorily represented by both model versions, or model performance is degraded with higher horizontal/vertical resolutions (Table S4). The model-observation mismatch may be explained by the following reasons. First, the prescribed monthly surface fluxes are probably not adequate to resolve the short-term variability at stations strongly influenced by local and regional sources, especially during the seasons when emissions from wetlands and rice paddies are active and temporally variable with temperature and moisture. Second, the sub-grid scale parameterizations in the current model we used are not able to realistically simulate the diurnal cycles of boundary layer mixing. Recently new physical parameterizations have been implemented in LMDz to better simulate vertical diffusion and mesoscale mixing by thermal plumes in the boundary layer (Hourdin et al., 2002; Rio et al., 2008), which can significantly improve simulation of the daily peak values during nighttime and thus diurnal cycles of tracer concentrations (Locatelli et al., 2015a).

Representation of the CH_4 diurnal cycle at mountain stations can be even more complicated, given that the mesoscale atmospheric transports such as mountain-vally circulations and terrain-induced up-down slope circulations cannot be resolved in global transport models (Griffiths et al., 2014; Pérez-Landa et al., 2007; Pillai et al., 2011). At BKT, a mountain station located on an altitude of 869 m a.s.l., the CH_4 diurnal cycle is not reasonably represented when model ouputs are sampled at the levels corresponding to this altitude (Level 3 and Level 4 for 19-layer and 39-layer models). The simulated CH_4 diurnal cycles sampled at a lower model level (Level 2 for both 19-layer and 39-layer models) agree much better

with the observed ones (Figure 5a). This suggests that the current model in use is not able to resolve mesoscale circulations in complex terrains, even with the zoomed grids (~50 km over the focal area) and 39 model layers.

3.4.2 CO_2 diurnal cycle

For CO_2, as shown in Figure 5b, the simulated diurnal cycles at GSN and PON correlate fairly well with the observed ones for their specific study periods (also see Table S5). The amplitudes of diurnal cycles are greatly underestimated, althougth this can be more or less improved with finer horizontal resolutions (Figure 5b). As for CH_4, the model-observation discrepencies mainly result from underestimated NEE diurnal cycles from ORCHIDEE and/or unresolved processes in the planetary boundary layer. Particularly, neither ZAs nor STs are able to adequately capture the CO_2 diurnal rectifier effect (Denning et al., 1996). For stations strongly influenced by local fossil fuel emissions, underestimation of the amplitudes may be additionally attributed to fine-scale sources not resolved at current horizontal resolutions. This is the case for PON, a coastal station 8 km north of the city of Pondicherry in India with a population of around 750,000 (Lin et al., 2015), where the amplitudes of diurnal cycles are underestimated for both CO_2 and CH_4 (Figure 5a,b). Again at BKT, as noted for CH_4, a better model-observation agreement is found for the CO_2 diurnal cycle when model outputs are sampled at the surface layer rather than the one corresponding to the station altitude (Figure 5b). Note that even the simulated diurnal cycles at the surface level are smaller compared to the observed ones by ~50%, suggesting that the diurnal variations of both NEE fluxes and terrain-induced circulations are probably not satisfactorily represented in the current simulations.

3.5 Evaluation against the CONTRAIL CO_2 vertical profiles

Figure 6 shows the simulated and observed CO_2 vertical profiles averaged for different seasons and over different regions. Over East Asia (EAS; Figure 6a and Figure S1), both ZAs and STs reasonably reproduce the shape of the observed CO_2 vertical profiles above 2 km, while below 2 km the magnitude of ΔCO_2 is significantly underestimated by up to 5 ppm. The simulated CO_2 vertical gradients between planetary boundary layer (BL) and free troposphere (FT) are lower than the observations by 2–3 ppm during winter (Figure 7a). The model-observation discrepancies are possibly due to stronger vertical mixing in LMDz (Locatelli et al., 2015a; Patra et al., 2011) as well as flux uncertainty. Note that as most

samples (79%) are taken over the Narita International Airport (NRT) and Chubu Centrair International Airport (NGO) in Japan located outside the zoomed region (Figure S1), STs slightly better capture the BL-FT gradients than ZAs.

Over the Indian sub-continent (IND, Figure 6b), there is large underestimation of the magnitude of ΔCO_2 near the surface by up to 8 ppm during April–June (AMJ), July–September (JAS) and October–December (OND). Accordingly, the BL-FT gradients are also underestimated by up to 3–4ppm for these periods (Figure 7b). The model-observation discrepancies are probably due to vertical mixing processes not realistically simulated in the current model (including deep convection), as well as the imperfect representation of CO_2 surface fluxes strongly influenced by the Indian monsoon system.

The CO_2 vertcial profiles over Southeast Asia (including Northern Southeast Asia (NSA) and Southern Southeast Asia (SSA)) are generally well reproduced (Figure 6c,d). However, both ZAs and STs fail to reproduce the BL-FT gradient of ~3 ppm in April for NSA (Figure 7c). Apart from errors due to vertical transport and/or prescribed NEE, inaccurate estimates of biomass burning emissions could also contribute to this model-observation mismatch.

Overall, the CO_2 vertical profiles in free troposphere are well simulated by both STs and ZAs over SEA, while significant underestimation of the BL-FT gradients is found for East Asia and the Indian sub-continent. The model-observation mismatch is due to misrepresentation of both vertical transport and prescribed surface fluxes, and can not be significantly reduced by solely refining the horizontal/vertical resolution, as shown by the very similar CO_2 vertical profiles simulated from ZAs and STs. New physical parameterization as shown in Locatelli et al., (2015a) should be implemented in the model to assess its potential to improve simulation of the vertical profiles of trace gases (especially the BL-FT gradients).

4 Conclusions and implications

In this study, we assess the capability of a global transport model (LMDzINCA) to simulate CH_4 and CO_2 variabilities over South and East Asia (SEA). Simulations have been performed with configurations of different horizontal (standard (STs) versus Asian zoom (ZAs)) and vertical (19 versus 39) resolutions. Model performance to represent trace gas variabilities is evaluated for each model version at multi-annual, seasonal, synoptic and diurnal scales,

against flask and continuous measurements from a unique dataset of 39 global and regional stations inside and outside the zoomed region. The evaluation at multiple temporal scales and comparisons between different model resolutions and trace gases have informed us of both advantages and challenges relating to high resolution transport modelling. Main conclusions and implications for possible model improvement and inverse modeling are summarized as follows.

First, ZAs improve the overall representation of CH_4 annual gradients between stations in SEA, with reduction of RMSE by 16–20% compared to STs. The model improvement mainly results from reduction in representation error with finer horizontal resolutions over SEA, through better characterization of CH_4 surface fluxes, transport, and/or topography around stations. Particularly, the scatterly distributed CH_4 emission sources (especially emission hotspots) can be more precisely defined with the Asian zoom grids, which makes the simulated concentration fields more heterogeneous, having the potential to improve representation of stations nearby on an annual basis.

However, as the model resolution increases, the simulated CH_4 concentration fields are more sensitive to possible errors in boundary conditions. Thus the performance of ZAs at a specific station as compared to STs depends on the accuracy and data quality of meteorological forcings and/or surface fluxes, especially when we examine short-term variabilities (synoptic and diurnal variations) or stations influenced by significant emission sources around. One example is UUM, at which ZAs even greatly degrade representation of synoptic variability due to presence of a wrong emission hotspot near the station in the EDGARv4.2FT2010 dataset. A sensitivity test prescribed with the improved emission dataset EDGARv4.3.2 show much better agreement with observations. This emphasizes importance of accurate a priori CH_4 surface fluxes in high resolution transport modelling and inversions, particularly regarding locations and magnitudes of emission hotspots. Any unrealistic emission hotspot close to a station (as shown for UUM) should be corrected before inversions, otherwise the inverted surface fluxes are likely to be strongly biased. Moreover, as current bottom-up estimates of CH_4 sources and sinks still suffer from large uncertainties at fine scales, caution should be taken when one attempts to assimilate observations not realistically simulated by the high resolution transport model. These observations should be either removed from inversions or allocated with large uncertainties.

With respect to CO_2, model performance and the limited model improvement with finer grids suggest that the CO_2 surface fluxes have not been prescribed with sufficient accuracy and resolution. One major component is NEE simulated from the terrestrial ecosystem model ORCHIDEE. For example, the smaller CO_2 seasonal amplitudes simulated at most inland stations in SEA mainly result from underestimated carbon uptake in northern mid-latitudes by ORCHIDEE, while the misrepresentation of synoptic and diurnal variabilities (especially for tropical stations like BKT and PON) is related to the inability of ORCHIDEE to satisfactorily capture sub-monthly to daily profiles of NEE. More efforts should be made to improve simulation of carbon exchange between land surface and atmosphere at various spatial and temporal scales.

Furthermore, apart from data quality of the prescribed surface fluxes, representation of the CH_4 and CO_2 short-term variabilities is also limited by model's ability to simulate boundary layer mixing and mesoscale transport in complex terrains. The recent implementation of new sub-grid physical parameterizations in LMDz is able to significantly improve simulation of the daily maximum during nighttime and thus diurnal cycles of tracer concentrations (Locatelli et al., 2015a). To fully take advantage of high-frequency CH_4 or CO_2 observations at stations close to source regions, it is highly recommended to implement the new boundary layer physics in the current transport model, in addition to refinement of model horizontal and vertical resolutions. The current transport model with old planetary boundary physics is not capable to capture diurnal variations at continental or mountain stations, therefore only observations that are well represented should be selected and kept for inversions (e.g. afternoon measurements for continental stations and nighttime measurements for mountain stations).

Lastly, the model-observation comparisons at multiple temporal scales can give us information about the magnitude of sources and sinks in the studied region. For example, at GSN, TAP and SDZ, all of which located in East and Northeast Asia, the CH_4 annual gradients as well as the amplitudes of seasonal and synoptic variability are consistently overestimated, suggesting overestimation of CH_4 emissions in East Asia. Therefore atmospheric inversions that assimilate information from these stations are expected to decrease emissions in East Asia, which agree with several recent global or regional studies from independent inventories (e.g., Peng et al., 2016) or inverse modeling (Bergamaschi et al., 2013; Bruhwiler et al., 2014; Thompson et al., 2015). Further studies are needed in the future

to estimate CH_4 budgets in SEA by utilizing high resolution transport models that are capable to represent regional networks of atmospheric observations.

Acknowledgement

This study was initiated within the framework of CaFICA-CEFIPRA project (2809-1). X. Lin acknowledges the PhD funding support from AIRBUS Defense & Space. P. Ciais thanks the ERC SyG project IMBALANCE-P 'Effects of Phosphorus Limitations on Life, Earth System and Society' Grant agreement (no. 610028). N. Evangeliou acknowledges the Nordic Center of Excellence eSTICC project (eScience Tools for Investigating Climate Change in northern high latitudes) funded by Nordforsk (no. 57001). We acknowledge the WDCGG for providing the archives of surface station observations for CO_2 and CH_4. We thank the following networks or institutes for the efforts on surface GHG measurements and their access: NOAA/ESRL, Aichi, BMKG, CMA, CSIR4PI, CSIRO, Empa, ESSO/NIOT, IIA, IITM, JMA, KMA, LSCE, NIER, NIES, PU and Saitama. We also thank Dr. T. Machida from NIES for providing CO_2 measurements from the CONTRAIL project. Finally, we would like to thank F. Marabelle and his team at LSCE, and the CURIE (TGCC) platform for the computing support.

References

Aalto, T., Hatakka, J., Karstens, U., Aurela, M., Thum, T. and Lohila, A.: Modeling atmospheric CO_2 concentration profiles and fluxes above sloping terrain at a boreal site, Atmos. Chem. Phys., 6(2), 303–314, doi:10.5194/acp-6-303-2006, 2006.

Aalto, T., Hatakka, J. and Lallo, M.: Tropospheric methane in northern Finland: seasonal variations, transport patterns and correlations with other trace gases, Tellus B, 59(2), 251–259, doi:10.1111/j.1600-0889.2007.00248.x, 2007.

Bakwin, P. S., Tans, P. P., Hurst, D. F. and Zhao, C.: Measurements of carbon dioxide on very tall towers: results of the NOAA/CMDL program, Tellus B, 50(5), 401–415, doi:10.1034/j.1600-0889.1998.t01-4-00001.x, 1998.

Berchet, A., Pison, I., Chevallier, F., Paris, J.-D., Bousquet, P., Bonne, J.-L., Arshinov, M. Y., Belan, B. D., Cressot, C., Davydov, D. K., Dlugokencky, E. J., Fofonov, A. V, Galanin, A., Lavrič, J., Machida, T., Parker, R., Sasakawa, M., Spahni, R., Stocker, B. D. and Winderlich, J.: Natural and anthropogenic methane fluxes in Eurasia: a mesoscale quantification by generalized atmospheric inversion, Biogeosciences, 12(18), 5393–5414, doi:10.5194/bg-12-5393-2015, 2015.

Bergamaschi, P., Corazza, M., Karstens, U., Athanassiadou, M., Thompson, R. L., Pison, I., Manning, A. J., Bousquet, P., Segers, A., Vermeulen, A. T., Janssens-Maenhout, G., Schmidt, M., Ramonet, M., Meinhardt, F., Aalto, T., Haszpra, L., Moncrieff, J., Popa, M. E., Lowry, D., Steinbacher, M., Jordan, A., O'Doherty, S., Piacentino, S. and Dlugokencky, E.: Top-down estimates of European CH_4 and N_2O emissions based on four different inverse models, Atmos. Chem. Phys., 15(2), 715–736, doi:10.5194/acp-15-715-2015, 2015.

Bergamaschi, P., Houweling, S., Segers, A., Krol, M., Frankenberg, C., Scheepmaker, R. A., Dlugokencky, E., Wofsy, S. C., Kort, E. A., Sweeney, C., Schuck, T., Brenninkmeijer, C., Chen, H., Beck, V. and Gerbig, C.: Atmospheric CH_4 in the first decade of the 21st century: Inverse modeling analysis using SCIAMACHY satellite retrievals and NOAA surface measurements, J. Geophys. Res. Atmos., 118(13), 7350–7369, doi:10.1002/jgrd.50480, 2013.

Bergamaschi, P., Krol, M., Dentener, F., Vermeulen, A., Meinhardt, F., Graul, R., Ramonet, M., Peters, W. and Dlugokencky, E. J.: Inverse modelling of national and European CH_4 emissions using the atmospheric zoom model TM5, Atmos. Chem. Phys., 5(9), 2431–2460, doi:10.5194/acp-5-2431-2005, 2005.

Bergamaschi, P., Krol, M., Meirink, J. F., Dentener, F., Segers, A., van Aardenne, J., Monni, S., Vermeulen, A. T., Schmidt, M., Ramonet, M., Yver, C., Meinhardt, F., Nisbet, E. G., Fisher, R. E., O'Doherty, S. and Dlugokencky, E. J.: Inverse modeling of European CH_4 emissions 2001–2006, J. Geophys. Res. Atmos., 115(D22), D22309, doi:10.1029/2010JD014180, 2010.

Bhattacharya, S. K., Borole, D. V, Francey, R. J., Allison, C. E., Steele, L. P., Krummel, P., Langenfelds, R., Masarie, K. A., Tiwari, Y. K. and Patra, P. K.: Trace gases and CO_2 isotope records from Cabo de Rama, India, Curr. Sci., 97(9), 1336–1344, 2009.

Boden, T. A., Marland, G. and Andres, R. J.: Global, Regional, and National Fossil-Fuel CO_2 Emissions, Oak Ridge, Tenn., USA., 2015.

Bousquet, P., Ciais, P., Miller, J. B., Dlugokencky, E. J., Hauglustaine, D. A., Prigent, C.,

Van der Werf, G. R., Peylin, P., Brunke, E.-G., Carouge, C., Langenfelds, R. L., Lathiere, J., Papa, F., Ramonet, M., Schmidt, M., Steele, L. P., Tyler, S. C. and White, J.: Contribution of anthropogenic and natural sources to atmospheric methane variability, Nature, 443(7110), 439–443 [online] Available from: http://dx.doi.org/10.1038/nature05132, 2006.

Bousquet, P., Peylin, P., Ciais, P., Le Quéré, C., Friedlingstein, P. and Tans, P. P.: Regional changes in carbon dioxide fluxes of land and oceans since 1980, Science (80-.)., 290(5495), 1342–1346 [online] Available from: http://science.sciencemag.org/content/290/5495/1342.abstract, 2000.

Bruhwiler, L., Dlugokencky, E., Masarie, K., Ishizawa, M., Andrews, A., Miller, J., Sweeney, C., Tans, P. and Worthy, D.: CarbonTracker-CH_4: an assimilation system for estimating emissions of atmospheric methane, Atmos. Chem. Phys., 14(16), 8269–8293, doi:10.5194/acp-14-8269-2014, 2014.

Cadule, P., Friedlingstein, P., Bopp, L., Sitch, S., Jones, C. D., Ciais, P., Piao, S. L. and Peylin, P.: Benchmarking coupled climate-carbon models against long-term atmospheric CO_2 measurements, Global Biogeochem. Cycles, 24(2), GB2016, doi:10.1029/2009GB003556, 2010.

Chen, Y.-H. and Prinn, R. G.: Atmospheric modeling of high- and low-frequency methane observations: Importance of interannually varying transport, J. Geophys. Res. Atmos., 110(D10), D10303, doi:10.1029/2004JD005542, 2005.

Chevillard, A., Karstens, U. T. E., Ciais, P., Lafont, S. and Heimann, M.: Simulation of atmospheric CO_2 over Europe and western Siberia using the regional scale model REMO, Tellus B, 54(5), 872–894, doi:10.1034/j.1600-0889.2002.01340.x, 2002.

Denning, A. S., Fung, I. Y. and Randall, D.: Latitudinal gradient of atmospheric CO2 due to seasonal exchange with land biota, Nature, 376(6537), 240–243, doi:10.1038/376240a0, 1995.

Denning, A. S., Randall, D. A., Collatz, G. J. and Sellers, P. J.: Simulations of terrestrial carbon metabolism and atmospheric CO_2 in a general circulation model, Tellus B, 48(4), 543–567, doi:10.1034/j.1600-0889.1996.t01-1-00010.x, 1996.

Fang, S., Tans, P. P., Dong, F., Zhou, H. and Luan, T.: Characteristics of atmospheric CO_2 and CH_4 at the Shangdianzi regional background station in China, Atmos. Environ., 131, 1–8, doi:http://dx.doi.org/10.1016/j.atmosenv.2016.01.044, 2016.

Fang, S. X., Zhou, L. X., Tans, P. P., Ciais, P., Steinbacher, M., Xu, L. and Luan, T.: In situ measurement of atmospheric CO_2 at the four WMO/GAW stations in China, Atmos. Chem. Phys., 14(5), 2541–2554, doi:10.5194/acp-14-2541-2014, 2014.

Feng, L., Palmer, P. I., Yang, Y., Yantosca, R. M., Kawa, S. R., Paris, J.-D., Matsueda, H. and Machida, T.: Evaluating a 3-D transport model of atmospheric CO_2 using ground-based, aircraft, and space-borne data, Atmos. Chem. Phys., 11(6), 2789–2803, doi:10.5194/acp-11-2789-2011, 2011.

Folberth, G. A., Hauglustaine, D. A., Lathière, J. and Brocheton, F.: Interactive chemistry in the Laboratoire de Météorologie Dynamique general circulation model: model description and impact analysis of biogenic hydrocarbons on tropospheric chemistry, Atmos. Chem. Phys., 6(8), 2273–2319, doi:10.5194/acp-6-2273-2006, 2006.

Ganesan, A. L., Chatterjee, A., Prinn, R. G., Harth, C. M., Salameh, P. K., Manning, A. J., Hall, B. D., Mühle, J., Meredith, L. K., Weiss, R. F., O'Doherty, S. and Young, D.: The

variability of methane, nitrous oxide and sulfur hexafluoride in Northeast India, Atmos. Chem. Phys., 13(21), 10633–10644, doi:10.5194/acp-13-10633-2013, 2013.

Geels, C., Doney, S. C., Dargaville, R., Brandt, J. and Christensen, J. H.: Investigating the sources of synoptic variability in atmospheric CO_2 measurements over the Northern Hemisphere continents: a regional model study, Tellus B, 56(1), 35–50, doi:10.1111/j.1600-0889.2004.00084.x, 2004.

Geels, C., Gloor, M., Ciais, P., Bousquet, P., Peylin, P., Vermeulen, A. T., Dargaville, R., Aalto, T., Brandt, J., Christensen, J. H., Frohn, L. M., Haszpra, L., Karstens, U., Rödenbeck, C., Ramonet, M., Carboni, G. and Santaguida, R.: Comparing atmospheric transport models for future regional inversions over Europe – Part 1: mapping the atmospheric CO2 signals, Atmos. Chem. Phys., 7(13), 3461–3479, doi:10.5194/acp-7-3461-2007, 2007a.

Geels, C., Gloor, M., Ciais, P., Bousquet, P., Peylin, P., Vermeulen, A. T., Dargaville, R., Aalto, T., Brandt, J., Christensen, J. H., Frohn, L. M., Haszpra, L., Karstens, U., Rödenbeck, C., Ramonet, M., Carboni, G. and Santaguida, R.: Comparing atmospheric transport models for future regional inversions over Europe – Part 1: mapping the atmospheric CO_2 signals, Atmos. Chem. Phys., 7(13), 3461–3479, doi:10.5194/acp-7-3461-2007, 2007b.

Griffiths, A. D., Conen, F., Weingartner, E., Zimmermann, L., Chambers, S. D., Williams, A. G. and Steinbacher, M.: Surface-to-mountaintop transport characterised by radon observations at the Jungfraujoch, Atmos. Chem. Phys., 14(23), 12763–12779, doi:10.5194/acp-14-12763-2014, 2014.

Gurney, K. R., Law, R. M., Denning, A. S., Rayner, P. J., Baker, D., Bousquet, P., Bruhwiler, L., Chen, Y.-H., Ciais, P., Fan, S., Fung, I. Y., Gloor, M., Heimann, M., Higuchi, K., John, J., Maki, T., Maksyutov, S., Masarie, K., Peylin, P., Prather, M., Pak, B. C., Randerson, J., Sarmiento, J., Taguchi, S., Takahashi, T. and Yuen, C.-W.: Towards robust regional estimates of CO_2 sources and sinks using atmospheric transport models, Nature, 415(6872), 626–630 [online] Available from: http://dx.doi.org/10.1038/415626a, 2002.

Hauglustaine, D. A., Balkanski, Y. and Schulz, M.: A global model simulation of present and future nitrate aerosols and their direct radiative forcing of climate, Atmos. Chem. Phys., 14(20), 11031–11063, doi:10.5194/acp-14-11031-2014, 2014.

Hauglustaine, D. A., Hourdin, F., Jourdain, L., Filiberti, M.-A., Walters, S., Lamarque, J.-F. and Holland, E. A.: Interactive chemistry in the Laboratoire de Météorologie Dynamique general circulation model: Description and background tropospheric chemistry evaluation, J. Geophys. Res. Atmos., 109(D4), D04314, doi:10.1029/2003JD003957, 2004.

Hourdin, F., Couvreux, F., Menut, L., Hourdin, F., Couvreux, F. and Menut, L.: Parameterization of the Dry Convective Boundary Layer Based on a Mass Flux Representation of Thermals, J. Atmos. Sci., 59(6), 1105–1123, doi:10.1175/1520-0469(2002)059<1105:POTDCB>2.0.CO;2, 2002.

Hourdin, F. and Issartel, J.-P.: Sub-surface nuclear tests monitoring through the CTBT Xenon Network, Geophys. Res. Lett., 27(15), 2245–2248, doi:10.1029/1999GL010909, 2000.

Hourdin, F., Musat, I., Bony, S., Braconnot, P., Codron, F., Dufresne, J.-L., Fairhead, L., Filiberti, M.-A., Friedlingstein, P., Grandpeix, J.-Y., Krinner, G., LeVan, P., Li, Z.-X. and Lott, F.: The LMDZ4 general circulation model: climate performance and sensitivity to parametrized physics with emphasis on tropical convection, Clim. Dyn., 27(7–8), 787–813, doi:10.1007/s00382-006-0158-0, 2006.

836 Houweling, S., Badawy, B., Baker, D. F., Basu, S., Belikov, D., Bergamaschi, P., Bousquet,
837 P., Broquet, G., Butler, T., Canadell, J. G., Chen, J., Chevallier, F., Ciais, P., Collatz, G. J.,
838 Denning, S., Engelen, R., Enting, I. G., Fischer, M. L., Fraser, A., Gerbig, C., Gloor, M.,
839 Jacobson, A. R., Jones, D. B. A., Heimann, M., Khalil, A., Kaminski, T., Kasibhatla, P. S.,
840 Krakauer, N. Y., Krol, M., Maki, T., Maksyutov, S., Manning, A., Meesters, A., Miller, J. B.,
841 Palmer, P. I., Patra, P., Peters, W., Peylin, P., Poussi, Z., Prather, M. J., Randerson, J. T.,
842 Röckmann, T., Rödenbeck, C., Sarmiento, J. L., Schimel, D. S., Scholze, M., Schuh, A.,
843 Suntharalingam, P., Takahashi, T., Turnbull, J., Yurganov, L. and Vermeulen, A.: Iconic
844 CO2 Time Series at Risk, Science (80-.)., 337(6098), 1038–1040 [online] Available from:
845 http://science.sciencemag.org/content/337/6098/1038.2.abstract, 2012.

846 Huntzinger, D. N., Schwalm, C., Michalak, A. M., Schaefer, K., King, A. W., Wei, Y.,
847 Jacobson, A., Liu, S., Cook, R. B., Post, W. M., Berthier, G., Hayes, D., Huang, M., Ito, A.,
848 Lei, H., Lu, C., Mao, J., Peng, C. H., Peng, S., Poulter, B., Riccuito, D., Shi, X., Tian, H.,
849 Wang, W., Zeng, N., Zhao, F. and Zhu, Q.: The North American Carbon Program Multi-
850 Scale Synthesis and Terrestrial Model Intercomparison Project – Part 1: Overview and
851 experimental design, Geosci. Model Dev., 6(6), 2121–2133, doi:10.5194/gmd-6-2121-2013,
852 2013.

853 JMA and WMO: WMO WDCGG Data Summary (WDCGG No. 38) Volume IV -
854 Greenhouse Gases and other Atmospheric Gases. [online] Available from:
855 http://ds.data.jma.go.jp/gmd/wdcgg/pub/products/summary/sum38/sum38.pdf, 2014.

856 Kaplan, J. O., Folberth, G. and Hauglustaine, D. A.: Role of methane and biogenic volatile
857 organic compound sources in late glacial and Holocene fluctuations of atmospheric methane
858 concentrations, Global Biogeochem. Cycles, 20(2), GB2016, doi:10.1029/2005GB002590,
859 2006.

860 Krol, M., Houweling, S., Bregman, B., van den Broek, M., Segers, A., van Velthoven, P.,
861 Peters, W., Dentener, F. and Bergamaschi, P.: The two-way nested global chemistry-transport
862 zoom model TM5: algorithm and applications, Atmos. Chem. Phys., 5(2), 417–432,
863 doi:10.5194/acp-5-417-2005, 2005.

864 Lambert, G. and Schmidt, S.: Reevaluation of the oceanic flux of methane: Uncertainties and
865 long term variations, Chemosphere, 26(1–4), 579–589, doi:http://dx.doi.org/10.1016/0045-
866 6535(93)90443-9, 1993.

867 Law, R. M., Peters, W., Rödenbeck, C., Aulagnier, C., Baker, I., Bergmann, D. J., Bousquet,
868 P., Brandt, J., Bruhwiler, L., Cameron-Smith, P. J., Christensen, J. H., Delage, F., Denning, A.
869 S., Fan, S., Geels, C., Houweling, S., Imasu, R., Karstens, U., Kawa, S. R., Kleist, J., Krol, M.
870 C., Lin, S.-J., Lokupitiya, R., Maki, T., Maksyutov, S., Niwa, Y., Onishi, R., Parazoo, N.,
871 Patra, P. K., Pieterse, G., Rivier, L., Satoh, M., Serrar, S., Taguchi, S., Takigawa, M.,
872 Vautard, R., Vermeulen, A. T. and Zhu, Z.: TransCom model simulations of hourly
873 atmospheric CO2: Experimental overview and diurnal cycle results for 2002, Global
874 Biogeochem. Cycles, 22(3), GB3009, doi:10.1029/2007GB003050, 2008.

875 Law, R. M., Rayner, P. J., Denning, A. S., Erickson, D., Fung, I. Y., Heimann, M., Piper, S.
876 C., Ramonet, M., Taguchi, S., Taylor, J. A., Trudinger, C. M. and Watterson, I. G.:
877 Variations in modeled atmospheric transport of carbon dioxide and the consequences for CO_2
878 inversions, Global Biogeochem. Cycles, 10(4), 783–796, doi:10.1029/96GB01892, 1996.

879 Levin, I., Ciais, P., Langenfelds, R., Schmidt, M., Ramonet, M., Sidorov, K., Tchebakova, N.,
880 Gloor, M., Heimann, M., Schulze, E.-D., Vygodskaya, N. N., Shibistova, O. and Lloyd, J.:

Three years of trace gas observations over the EuroSiberian domain derived from aircraft sampling — a concerted action, Tellus B, 54(5), 696–712, doi:10.1034/j.1600-0889.2002.01352.x, 2002.

Lin, X., Indira, N. K., Ramonet, M., Delmotte, M., Ciais, P., Bhatt, B. C., Reddy, M. V, Angchuk, D., Balakrishnan, S., Jorphail, S., Dorjai, T., Mahey, T. T., Patnaik, S., Begum, M., Brenninkmeijer, C., Durairaj, S., Kirubagaran, R., Schmidt, M., Swathi, P. S., Vinithkumar, N. V, Yver Kwok, C. and Gaur, V. K.: Long-lived atmospheric trace gases measurements in flask samples from three stations in India, Atmos. Chem. Phys., 15(17), 9819–9849, doi:10.5194/acp-15-9819-2015, 2015.

Locatelli, R.: Estimation des sources et puits de méthane: bilan planétaire et impacts de la modélisation du transport atmosphérique, Versailles-St Quentin en Yvelines, France. [online] Available from: http://www.theses.fr/2014VERS0035, 2014.

Locatelli, R., Bousquet, P., Chevallier, F., Fortems-Cheney, A., Szopa, S., Saunois, M., Agusti-Panareda, A., Bergmann, D., Bian, H., Cameron-Smith, P., Chipperfield, M. P., Gloor, E., Houweling, S., Kawa, S. R., Krol, M., Patra, P. K., Prinn, R. G., Rigby, M., Saito, R. and Wilson, C.: Impact of transport model errors on the global and regional methane emissions estimated by inverse modelling, Atmos. Chem. Phys., 13(19), 9917–9937, doi:10.5194/acp-13-9917-2013, 2013.

Locatelli, R., Bousquet, P., Hourdin, F., Saunois, M., Cozic, A., Couvreux, F., Grandpeix, J.-Y., Lefebvre, M.-P., Rio, C., Bergamaschi, P., Chambers, S. D., Karstens, U., Kazan, V., van der Laan, S., Meijer, H. A. J., Moncrieff, J., Ramonet, M., Scheeren, H. A., Schlosser, C., Schmidt, M., Vermeulen, A. and Williams, A. G.: Atmospheric transport and chemistry of trace gases in LMDz5B: evaluation and implications for inverse modelling, Geosci. Model Dev., 8(2), 129–150, doi:10.5194/gmd-8-129-2015, 2015a.

Locatelli, R., Bousquet, P., Saunois, M., Chevallier, F. and Cressot, C.: Sensitivity of the recent methane budget to LMDz sub-grid-scale physical parameterizations, Atmos. Chem. Phys, 15, 9765–9780, doi:10.5194/acp-15-9765-2015, 2015b.

Lopez, M., Schmidt, M., Ramonet, M., Bonne, J.-L., Colomb, A., Kazan, V., Laj, P. and Pichon, J.-M.: Three years of semicontinuous greenhouse gas measurements at the Puy de Dôme station (central France), Atmos. Meas. Tech., 8(9), 3941–3958, doi:10.5194/amt-8-3941-2015, 2015.

Louis, J.-F.: A parametric model of vertical eddy fluxes in the atmosphere, Boundary-Layer Meteorol., 17(2), 187–202, doi:10.1007/BF00117978, 1979.

Machida, T., Katsumata, K., Tohjima, Y., Watai, T. and Mukai, H.: Preparing and maintaining of CO_2 calibration scale in National Institute for Environmental Studies: NIES 95 CO_2 scale, in Report of the 14th WMO/IAEA Meeting of Experts on Carbon Dioxide Concentration and Related Tracer Measurement Techniques, edited by T. Laurila, pp. 26–29, GMO/GAW Report No. 186, Helsinki., 2009.

Machida, T., Matsueda, H., Sawa, Y., Nakagawa, Y., Hirotani, K., Kondo, N., Goto, K., Nakazawa, T., Ishikawa, K. and Ogawa, T.: Worldwide measurements of atmospheric CO_2 and other trace gas species using commercial airlines, J. Atmos. Ocean. Technol., 25(10), 1744–1754, doi:10.1175/2008JTECHA1082.1, 2008.

Maksyutov, S., Patra, P. K., Onishi, R., Saeki, T. and Nakazawa, T.: NIES/FRCGC Global Atmospheric Tracer Transport Model: Description, validation, and surfae sources and sinks

925 inversion, J. Earth Simulator, 9, 3–18, 2008.

926 Matthews, E., Fung, I. and Lerner, J.: Methane emission from rice cultivation: Geographic
927 and seasonal distribution of cultivated areas and emissions, Global Biogeochem. Cycles, 5(1),
928 3–24, doi:10.1029/90GB02311, 1991.

929 Miles, N. L., Richardson, S. J., Davis, K. J., Lauvaux, T., Andrews, A. E., West, T. O.,
930 Bandaru, V. and Crosson, E. R.: Large amplitude spatial and temporal gradients in
931 atmospheric boundary layer CO_2 mole fractions detected with a tower-based network in the
932 U.S. upper Midwest, J. Geophys. Res. Biogeosciences, 117(G1), n/a-n/a,
933 doi:10.1029/2011JG001781, 2012.

934 Olivier, J. G. J., Janssens-Maenhout, G., Muntean, M. and Peters, J. A. H. W.: Trends in
935 global CO_2 emissions: 2015 Report., 2015.

936 Parazoo, N. C., Denning, A. S., Kawa, S. R., Corbin, K. D., Lokupitiya, R. S. and Baker, I. T.:
937 Mechanisms for synoptic variations of atmospheric CO_2 in North America, South America
938 and Europe, Atmos. Chem. Phys., 8(23), 7239–7254, doi:10.5194/acp-8-7239-2008, 2008.

939 Park, G., Wanninkhof, R. I. F., Doney, S. C., Takahashi, T., Lee, K., Feely, R. A., Sabine, C.
940 L., Triñanes, J. and Lima, I. D.: Variability of global net sea–air CO_2 fluxes over the last
941 three decades using empirical relationships, Tellus B, 62(5), 352–368, doi:10.1111/j.1600-
942 0889.2010.00498.x, 2010.

943 Patra, P. K., Canadell, J. G., Houghton, R. A., Piao, S. L., Oh, N.-H., Ciais, P., Manjunath, K.
944 R., Chhabra, A., Wang, T., Bhattacharya, T., Bousquet, P., Hartman, J., Ito, A., Mayorga, E.,
945 Niwa, Y., Raymond, P. A., Sarma, V. V. S. S. and Lasco, R.: The carbon budget of South
946 Asia, Biogeosciences, 10(1), 513–527, doi:10.5194/bg-10-513-2013, 2013.

947 Patra, P. K., Houweling, S., Krol, M., Bousquet, P., Belikov, D., Bergmann, D., Bian, H.,
948 Cameron-Smith, P., Chipperfield, M. P., Corbin, K., Fortems-Cheiney, A., Fraser, A., Gloor,
949 E., Hess, P., Ito, A., Kawa, S. R., Law, R. M., Loh, Z., Maksyutov, S., Meng, L., Palmer, P. I.,
950 Prinn, R. G., Rigby, M., Saito, R. and Wilson, C.: TransCom model simulations of CH4 and
951 related species: linking transport, surface flux and chemical loss with CH_4 variability in the
952 troposphere and lower stratosphere, Atmos. Chem. Phys., 11(24), 12813–12837,
953 doi:10.5194/acp-11-12813-2011, 2011.

954 Patra, P. K., Law, R. M., Peters, W., Rödenbeck, C., Takigawa, M., Aulagnier, C., Baker, I.,
955 Bergmann, D. J., Bousquet, P., Brandt, J., Bruhwiler, L., Cameron-Smith, P. J., Christensen, J.
956 H., Delage, F., Denning, A. S., Fan, S., Geels, C., Houweling, S., Imasu, R., Karstens, U.,
957 Kawa, S. R., Kleist, J., Krol, M. C., Lin, S.-J., Lokupitiya, R., Maki, T., Maksyutov, S., Niwa,
958 Y., Onishi, R., Parazoo, N., Pieterse, G., Rivier, L., Satoh, M., Serrar, S., Taguchi, S.,
959 Vautard, R., Vermeulen, A. T. and Zhu, Z.: TransCom model simulations of hourly
960 atmospheric CO2: Analysis of synoptic-scale variations for the period 2002–2003, Global
961 Biogeochem. Cycles, 22(4), GB4013, doi:10.1029/2007GB003081, 2008.

962 Patra, P. K., Takigawa, M., Dutton, G. S., Uhse, K., Ishijima, K., Lintner, B. R., Miyazaki, K.
963 and Elkins, J. W.: Transport mechanisms for synoptic, seasonal and interannual SF_6
964 variations and "age" of air in troposphere, Atmos. Chem. Phys., 9(4), 1209–1225,
965 doi:10.5194/acp-9-1209-2009, 2009a.

966 Patra, P., Takigawa, M., Ishijima, K., Choi, B.-C., Cunnold, D., J. Dlugokencky, E., Fraser,
967 P., J. Gomez-Pelaez, A., Goo, T.-Y., Kim, J.-S., Krummel, P., Langenfelds, R., Meinhardt, F.,
968 Mukai, H., O'Doherty, S., G. Prinn, R., Simmonds, P., Steele, P., Tohjima, Y., Tsuboi, K.,

969 Uhse, K., Weiss, R., Worthy, D. and Nakazawa, T.: Growth rate, seasonal, synoptic, diurnal
970 variations and budget of methane in the lower atmosphere, J. Meteorol. Soc. Japan. Ser. II,
971 87(4), 635–663, 2009b.

972 Peng, S., Ciais, P., Chevallier, F., Peylin, P., Cadule, P., Sitch, S., Piao, S., Ahlström, A.,
973 Huntingford, C., Levy, P., Li, X., Liu, Y., Lomas, M., Poulter, B., Viovy, N., Wang, T.,
974 Wang, X., Zaehle, S., Zeng, N., Zhao, F. and Zhao, H.: Benchmarking the seasonal cycle of
975 CO_2 fluxes simulated by terrestrial ecosystem models, Global Biogeochem. Cycles, 29(1),
976 46–64, doi:10.1002/2014GB004931, 2015.

977 Peng, S. S., Piao, S. L., Bousquet, P., Ciais, P., Li, B. G., Lin, X., Tao, S., Wang, Z. P.,
978 Zhang, Y. and Zhou, F.: Inventory of anthropogenic methane emissions in Mainland China
979 from 1980 to 2010, Atmos. Chem. Phys. Discuss., 2016, 1–29, doi:10.5194/acp-2016-139,
980 2016.

981 Pérez-Landa, G., Ciais, P., Sanz, M. J., Gioli, B., Miglietta, F., Palau, J. L., Gangoiti, G. and
982 Millán, M. M.: Mesoscale circulations over complex terrain in the Valencia coastal region,
983 Spain – Part 1: Simulation of diurnal circulation regimes, Atmos. Chem. Phys., 7(7), 1835–
984 1849, doi:10.5194/acp-7-1835-2007, 2007.

985 Peters, W., Krol, M. C., Dlugokencky, E. J., Dentener, F. J., Bergamaschi, P., Dutton, G.,
986 Velthoven, P. v., Miller, J. B., Bruhwiler, L. and Tans, P. P.: Toward regional-scale modeling
987 using the two-way nested global model TM5: Characterization of transport using SF_6, J.
988 Geophys. Res. Atmos., 109(D19), D19314, doi:10.1029/2004JD005020, 2004.

989 Peters, W., Krol, M. C., Van Der Werf, G. R., Houweling, S., Jones, C. D., Hughes, J.,
990 Schaefer, K., Masarie, K. A., Jacobson, A. R., Miller, J. B., Cho, C. H., Ramonet, M.,
991 Schmidt, M., Ciattaglia, L., Apadula, F., Heltai, D., Meinhardt, F., Di Sarra, A. G., Piacentino,
992 S., Sferlazzo, D., Aalto, T., Hatakka, J., StrÖm, J., Haszpra, L., Meijer, H. A. J., Van der
993 Laan, S., Neubert, R. E. M., Jordan, A., RodÓ, X., MorguÍ, J.-A., Vermeulen, A. T., Popa, E.,
994 Rozanski, K., Zimnoch, M., Manning, A. C., Leuenberger, M., Uglietti, C., Dolman, A. J.,
995 Ciais, P., Heimann, M. and Tans, P. P.: Seven years of recent European net terrestrial carbon
996 dioxide exchange constrained by atmospheric observations, Glob. Chang. Biol., 16(4), 1317–
997 1337, doi:10.1111/j.1365-2486.2009.02078.x, 2010.

998 Pillai, D., Gerbig, C., Ahmadov, R., Rödenbeck, C., Kretschmer, R., Koch, T., Thompson, R.,
999 Neininger, B. and Lavrié, J. V: High-resolution simulations of atmospheric CO_2 over
1000 complex terrain – representing the Ochsenkopf mountain tall tower, Atmos. Chem. Phys.,
1001 11(15), 7445–7464, doi:10.5194/acp-11-7445-2011, 2011.

1002 Popa, M. E., Gloor, M., Manning, A. C., Jordan, A., Schultz, U., Haensel, F., Seifert, T. and
1003 Heimann, M.: Measurements of greenhouse gases and related tracers at Bialystok tall tower
1004 station in Poland, Atmos. Meas. Tech., 3(2), 407–427, doi:10.5194/amt-3-407-2010, 2010.

1005 Pregger, T., Scholz, Y. and Friedrich, R.: Documentation of the anthropogenic GHG
1006 emission data for Europe provided in the Frame of CarboEurope GHG and CarboEurope IP,
1007 Stuttgart, Germany., 2007.

1008 Le Quéré, C., Moriarty, R., Andrew, R. M., Canadell, J. G., Sitch, S., Korsbakken, J. I.,
1009 Friedlingstein, P., Peters, G. P., Andres, R. J., Boden, T. A., Houghton, R. A., House, J. I.,
1010 Keeling, R. F., Tans, P., Arneth, A., Bakker, D. C. E., Barbero, L., Bopp, L., Chang, J.,
1011 Chevallier, F., Chini, L. P., Ciais, P., Fader, M., Feely, R. A., Gkritzalis, T., Harris, I., Hauck,
1012 J., Ilyina, T., Jain, A. K., Kato, E., Kitidis, V., Klein Goldewijk, K., Koven, C., Landschützer,

P., Lauvset, S. K., Lefèvre, N., Lenton, A., Lima, I. D., Metzl, N., Millero, F., Munro, D. R., Murata, A., Nabel, J. E. M. S., Nakaoka, S., Nojiri, Y., O'Brien, K., Olsen, A., Ono, T., Pérez, F. F., Pfeil, B., Pierrot, D., Poulter, B., Rehder, G., Rödenbeck, C., Saito, S., Schuster, U., Schwinger, J., Séférian, R., Steinhoff, T., Stocker, B. D., Sutton, A. J., Takahashi, T., Tilbrook, B., van der Laan-Luijkx, I. T., van der Werf, G. R., van Heuven, S., Vandemark, D., Viovy, N., Wiltshire, A., Zaehle, S. and Zeng, N.: Global Carbon Budget 2015, Earth Syst. Sci. Data, 7(2), 349–396, doi:10.5194/essd-7-349-2015, 2015.

Ramonet, M., Ciais, P., Nepomniachii, I., Sidorov, K., Neubert, R. E. M., Langendörfer, U., Picard, D., Kazan, V., Biraud, S., Gusti, M., Kolle, O., Schulze, E.-D. and Lloyd, J.: Three years of aircraft-based trace gas measurements over the Fyodorovskoye southern taiga forest, 300 km north-west of Moscow, Tellus B, 54(5), 713–734, doi:10.1034/j.1600-0889.2002.01358.x, 2002.

Randerson, J. T., Chen, Y., van der Werf, G. R., Rogers, B. M. and Morton, D. C.: Global burned area and biomass burning emissions from small fires, J. Geophys. Res. Biogeosciences, 117(G4), n/a-n/a, doi:10.1029/2012JG002128, 2012.

Ridgwell, A. J., Marshall, S. J. and Gregson, K.: Consumption of atmospheric methane by soils: A process-based model, Global Biogeochem. Cycles, 13(1), 59–70, doi:10.1029/1998GB900004, 1999.

Rio, C., Hourdin, F., Rio, C. and Hourdin, F.: A Thermal Plume Model for the Convective Boundary Layer: Representation of Cumulus Clouds, J. Atmos. Sci., 65(2), 407–425, doi:10.1175/2007JAS2256.1, 2008.

Rödenbeck, C., Houweling, S., Gloor, M. and Heimann, M.: CO_2 flux history 1982–2001 inferred from atmospheric data using a global inversion of atmospheric transport, Atmos. Chem. Phys., 3(6), 1919–1964, doi:10.5194/acp-3-1919-2003, 2003.

Saeki, T., Saito, R., Belikov, D. and Maksyutov, S.: Global high-resolution simulations of CO2 and CH4 using a NIES transport model to produce a priori concentrations for use in satellite data retrievals, Geosci. Model Dev., 6(1), 81–100, doi:10.5194/gmd-6-81-2013, 2013.

Sanderson, M. G.: Biomass of termites and their emissions of methane and carbon dioxide: A global database, Global Biogeochem. Cycles, 10(4), 543–557, doi:10.1029/96GB01893, 1996.

Sasakawa, M., Shimoyama, K., Machida, T., Tsuda, N., Suto, H., Arshinov, M., Davydov, D., Fofonov, A., Krasnov, O., Saeki, T., Koyama, Y. and Maksyutov, S.: Continuous measurements of methane from a tower network over Siberia, Tellus B, 62(5), 403–416, doi:10.1111/j.1600-0889.2010.00494.x, 2010.

Swathi, P. S., Indira, N. K., Rayner, P. J., Ramonet, M., Jagadheesha, D., Bhatt, B. C. and Gaur, V. K.: Robust inversion of carbon dioxide fluxes over temperate Eurasia in 2006-2008, Curr. Sci., 105(2), 201–208, 2013.

Szopa, S., Balkanski, Y., Schulz, M., Bekki, S., Cugnet, D., Fortems-Cheiney, A., Turquety, S., Cozic, A., Déandreis, C., Hauglustaine, D., Idelkadi, A., Lathière, J., Lefevre, F., Marchand, M., Vuolo, R., Yan, N. and Dufresne, J.-L.: Aerosol and ozone changes as forcing for climate evolution between 1850 and 2100, Clim. Dyn., 40(9–10), 2223–2250, doi:10.1007/s00382-012-1408-y, 2013.

Taylor, K. E.: Summarizing multiple aspects of model performance in a single diagram, J. Geophys. Res. Atmos., 106(D7), 7183–7192, doi:10.1029/2000JD900719, 2001.

Thompson, R. L., Ishijima, K., Saikawa, E., Corazza, M., Karstens, U., Patra, P. K., Bergamaschi, P., Chevallier, F., Dlugokencky, E., Prinn, R. G., Weiss, R. F., O'Doherty, S., Fraser, P. J., Steele, L. P., Krummel, P. B., Vermeulen, A., Tohjima, Y., Jordan, A., Haszpra, L., Steinbacher, M., Van der Laan, S., Aalto, T., Meinhardt, F., Popa, M. E., Moncrieff, J. and Bousquet, P.: TransCom N_2O model inter-comparison – Part 2: Atmospheric inversion estimates of N_2O emissions, Atmos. Chem. Phys., 14(12), 6177–6194, doi:10.5194/acp-14-6177-2014, 2014.

Thompson, R. L., Patra, P. K., Chevallier, F., Maksyutov, S., Law, R. M., Ziehn, T., van der Laan-Luijkx, I. T., Peters, W., Ganshin, A., Zhuravlev, R., Maki, T., Nakamura, T., Shirai, T., Ishizawa, M., Saeki, T., Machida, T., Poulter, B., Canadell, J. G. and Ciais, P.: Top-down assessment of the Asian carbon budget since the mid 1990s, Nat Commun, 7 [online] Available from: http://dx.doi.org/10.1038/ncomms10724, 2016.

Thompson, R. L., Stohl, A., Zhou, L. X., Dlugokencky, E., Fukuyama, Y., Tohjima, Y., Kim, S.-Y., Lee, H., Nisbet, E. G., Fisher, R. E., Lowry, D., Weiss, R. F., Prinn, R. G., O'Doherty, S., Young, D. and White, J. W. C.: Methane emissions in East Asia for 2000–2011 estimated using an atmospheric Bayesian inversion, J. Geophys. Res. Atmos., 120(9), 4352–4369, doi:10.1002/2014JD022394, 2015.

Thoning, K. W., Tans, P. P. and Komhyr, W. D.: Atmospheric carbon dioxide at Mauna Loa Observatory: 2. Analysis of the NOAA GMCC data, 1974–1985, J. Geophys. Res. Atmos., 94(D6), 8549–8565, doi:10.1029/JD094iD06p08549, 1989.

Tian, H., Lu, C., Ciais, P., Michalak, A. M., Canadell, J. G., Saikawa, E., Huntzinger, D. N., Gurney, K. R., Sitch, S., Zhang, B., Yang, J., Bousquet, P., Bruhwiler, L., Chen, G., Dlugokencky, E., Friedlingstein, P., Melillo, J., Pan, S., Poulter, B., Prinn, R., Saunois, M., Schwalm, C. R. and Wofsy, S. C.: The terrestrial biosphere as a net source of greenhouse gases to the atmosphere, Nature, 531(7593), 225–228 [online] Available from: http://dx.doi.org/10.1038/nature16946, 2016.

Tiedtke, M.: A Comprehensive mass flux scheme for cumulus parameterization in large-scale models, Mon. Weather Rev., 117(8), 1779–1800, doi:10.1175/1520-0493(1989)117<1779:ACMFSF>2.0.CO, 1989.

Tiwari, Y. K. and Kumar, R. K.: GHG observation programs in India, Asian GAW Greenh. Gases Newsl., No.3, 5–11, 2012.

Tiwari, Y. K., Vellore, R. K., Ravi Kumar, K., van der Schoot, M. and Cho, C.-H.: Influence of monsoons on atmospheric CO_2 spatial variability and ground-based monitoring over India, Sci. Total Environ., 490(0), 570–578, doi:http://dx.doi.org/10.1016/j.scitotenv.2014.05.045, 2014.

Wada, A., Matsueda, H., Sawa, Y., Tsuboi, K. and Okubo, S.: Seasonal variation of enhancement ratios of trace gases observed over 10 years in the western North Pacific, Atmos. Environ., 45(12), 2129–2137, doi:http://dx.doi.org/10.1016/j.atmosenv.2011.01.043, 2011.

Wang, J.-W., Denning, A. S., Lu, L., Baker, I. T., Corbin, K. D. and Davis, K. J.: Observations and simulations of synoptic, regional, and local variations in atmospheric CO_2, J. Geophys. Res. Atmos., 112(D4), D04108, doi:10.1029/2006JD007410, 2007.

Wang, R., Balkanski, Y., Boucher, O., Ciais, P., Schuster, G. L., Chevallier, F., Samset, B. H., Liu, J., Piao, S., Valari, M. and Tao, S.: Estimation of global black carbon direct radiative forcing and its uncertainty constrained by observations, J. Geophys. Res. Atmos., 121(10),

5948–5971, doi:10.1002/2015JD024326, 2016.

Wang, R., Tao, S., Balkanski, Y., Ciais, P., Boucher, O., Liu, J., Piao, S., Shen, H., Vuolo, M. R., Valari, M., Chen, H., Chen, Y., Cozic, A., Huang, Y., Li, B., Li, W., Shen, G., Wang, B. and Zhang, Y.: Exposure to ambient black carbon derived from a unique inventory and high-resolution model, Proc. Natl. Acad. Sci. [online] Available from: http://www.pnas.org/content/early/2014/01/23/1318763111.abstract, 2014.

Wei, Y., Liu, S., Huntzinger, D. N., Michalak, A. M., Viovy, N., Post, W. M., Schwalm, C. R., Schaefer, K., Jacobson, A. R., Lu, C., Tian, H., Ricciuto, D. M., Cook, R. B., Mao, J. and Shi, X.: The North American Carbon Program Multi-scale Synthesis and Terrestrial Model Intercomparison Project – Part 2: Environmental driver data, Geosci. Model Dev., 7(6), 2875–2893, doi:10.5194/gmd-7-2875-2014, 2014.

Van Der Werf, G. R., Randerson, J. T., Giglio, L., Van Leeuwen, T. T., Chen, Y., Rogers, B. M., Mu, M., Van Marle, M. J. E., Morton, D. C., Collatz, G. J., Yokelson, R. J. and Kasibhatla, P. S.: Global fire emissions estimates during 1997–2016, Earth Syst. Sci. Data, 95194, 697–720, doi:10.5194/essd-9-697-2017, 2017.

Winderlich, J., Chen, H., Gerbig, C., Seifert, T., Kolle, O., Lavrič, J. V, Kaiser, C., Höfer, A. and Heimann, M.: Continuous low-maintenance CO_2/CH_4/H_2O measurements at the Zotino Tall Tower Observatory (ZOTTO) in Central Siberia, Atmos. Meas. Tech., 3(4), 1113–1128, doi:10.5194/amt-3-1113-2010, 2010.

Yver Kwok, C., Laurent, O., Guemri, A., Philippon, C., Wastine, B., Rella, C. W., Vuillemin, C., Truong, F., Delmotte, M., Kazan, V., Darding, M., Lebègue, B., Kaiser, C., Xueref-Rémy, I. and Ramonet, M.: Comprehensive laboratory and field testing of cavity ring-down spectroscopy analyzers measuring H_2O, CO_2, CH_4 and CO, Atmos. Meas. Tech., 8(9), 3867–3892, doi:10.5194/amt-8-3867-2015, 2015.

Tables

Table 1 The prescribed CH_4 and CO_2 surface fluxes used as model input. For each trace gas, magnitudes of different types of fluxes are given for the year 2010. $Total_{global}$ and $Total_{zoom}$ indicate the total flux summarized over the globe and the zoomed region, respectively.

Type of CH_4 fluxes	Temporal resolution	Spatial resolution	$Total_{global}$ ($TgCH_4/yr$)	$Total_{zoom}$ ($TgCH_4/yr$)	Data source
Anthropogenic – rice	Monthly, interannual	0.1°	38	32	EDGARv4.2FT2010 + Matthews et al (1991)
Anthropogenic – others	Yearly, interannual	0.1°	320	130	EDGARv4.2FT2010
Wetland	Monthly, climatological	1°	175	29	Kaplan et al. (2006)
Biomass burning	Monthly, interannual	0.5°	12	1	GFED v4.1
Termite	Monthly, climatological	1°	19	3	Sanderson et al. (1996)
Soil	Monthly, climatological	1°	-38	-7	Ridgwell et al. (1999)
Ocean	Monthly, climatological	1°	17	3	Lambert & Schmidt (1993)
Total, $TgCH_4/yr$			543	191	
Type of CO_2 fluxes	Temporal resolution	Spatial resolution	$Total_{global}$ (PgC/yr)	$Total_{zoom}$ (PgC/yr)	Data source
Anthropogenic	Monthly, interannual Daily, interannual Hourly, interannual	1°	8.9	3.6	IER-EDGAR product
Biomass burning	Monthly, interannual	0.5°	2.0	0.2	GFED v4.1
Land flux (NEE)	Monthly, interannual Daily, interannual Hourly, interannual	0.5°	-2.7	0.1	OCHIDEE outputs from trunk version r1882
Ocean flux	Monthly, interannual	4°×5°	-1.3	0.1	NOAA/PMEL & AOML product; Park et al. (2010)
Total, PgC/yr			6.9	3.9	

1131 **Table 2** Stations used in this study. For the column 'Zoom', 'Y' indicates a station within the zoomed region.

	Code	Station	LON (°)	LAT (°)	ALT (masl)	Contributor	Type	Time periods used in this study	Zoom	CH_4	CO_2
1	ALT	Alert, Canada	-62.52	82.45	210	NOAA/ESRL	coastal	Flask: 2006–2013		Y	Y
2	AMS	Amsterdam Island, France	77.54	-37.80	70	LSCE	marine	Flask: 2006–2013		Y	Y
3	AMY	Anmyeon-do, Korea	126.32	36.53	133	KMA	coastal	Continuous: 2006–2013	Y	Y	
4	BKT	Bukit Kototabang, Indonesia	100.32	-0.20	869	BMKG, Empa, NOAA/ESRL	mountain	Flask: 2006–2013 CH_4 continuous: 2009–2013 CO_2 continuous: 2010–2013	Y	Y	Y
5	BRW	Barrow, USA	-156.60	71.32	11	NOAA/ESRL	coastal	Continuous: 2006–2013		Y	Y
6	CGO	Cape Grim, Australia	144.68	-40.68	94	NOAA/ESRL	marine	Flask: 2006–2013		Y	Y
7	COI	Cape Ochi-ishi, Japan	145.50	43.16	94	NIES	coastal	Continuous: 2006–2013		Y	
8	CRI	Cape Rama, India	73.83	15.08	66	CSIRO	coastal	Flask: 2009–2013	Y	Y	Y
9	DDR	Mt. Dodaira, Japan	139.18	36.00	840	Saitama	mountain	Continuous: 2006–2013			Y
10	DSI	Dongsha Island, Taiwan, China	116.73	20.70	8	National Central Univ., NOAA/ESRL	marine	Flask: 2010–2013	Y	Y	Y
11	GMI	Mariana Island, Guam	144.66	13.39	5	Univ. of Guam, NOAA/ESRL	marine	Flask: 2006–2013		Y	Y
12	GSN	Gosan, Korea	126.12	33.15	144	NIER	marine	Continous: 2006–2011	Y	Y	Y
13	HAT	Hateruma, Japan	123.81	24.06	47	NIES	marine	Continous: 2006–2013	Y	Y	
14	HLE	Hanle, India	78.96	32.78	4517	LSCE, CSIR4PI, IIA	mountain	Flask: 2006–2013 CH_4 continuous: 2012–2013 CO_2 continuous: 2006–2013	Y	Y	Y
15	JFJ	Jungfraujoch, Switzerland	7.99	46.55	3580	Empa	mountain	CH_4 continuous: 2006–2013 CO_2 continuous: 2010–2013		Y	Y
16	JIN	Jinsha, China	114.20	29.63	750	CMA	continental	Flask: 2006–2011	Y		Y
17	KIS	Kisai - Saitama	139.55	36.08	13	Saitama	continental	Continous: 2006–2013			Y
18	KZD	Sary Taukum, Kazakhstan	75.57	44.45	412	KSIEMC, NOAA/ESRL	continental	Flask: 2006–2009	Y	Y	Y
19	KZM	Plateau Assy, Kazakhstan	77.87	43.25	2524	KSIEMC, NOAA/ESRL	mountain	Flask: 2006–2009	Y	Y	Y
20	LIN	Lin'an, China	119.72	30.30	139	CMA	continental	Flask: 2006–2011	Y		Y
21	LLN	Lulin, Taiwan, China	120.87	23.47	2867	LAIBS, NOAA/ESRL	mountain	Flask: 2006–2013	Y	Y	Y
22	LON	Longfengshan, China	127.60	44.73	331	CMA	continental	Flask: 2006–2011	Y		Y
23	MHD	Mace Head, Ireland	-9.90	53.33	8	NOAA/ESRL	coastal	Flask: 2006–2013		Y	Y
24	MKW	Mikawa-Ichinomiya, Japan	137.43	34.85	50	Aichi	continental	Continous: 2006–2011	Y		Y

25	MLO	Mauna Loa, USA	-155.58	19.54	3397	NOAA/ESRL	mountain	Continuous: 2006–2013		Y	Y
26	MNM	Minamitori-shima, Japan	153.98	24.28	28	JMA	marine	Continuous: 2006–2013		Y	Y
27	NWR	Niwot Ridge, USA	-105.59	40.05	3523	NOAA/ESRL	mountain	Flask: 2006–2013		Y	Y
28	PBL	Port Blair, India	92.76	11.65	20	LSCE, CSIR4PI, ESSO/NIOT	marine	Flask: 2009–2013	Y	Y	Y
29	PON	Pondicherry, India	79.86	12.01	30	LSCE, CSIR4PI, Pondicherry Univ.	coastal	Flask: 2006–2013 CH_4 continuous: 2011–2013 CO_2 continuous: 2011–2013	Y	Y	Y
30	RYO	Ryori, Japan	141.82	39.03	280	JMA	continental	Continuous: 2006–2013		Y	Y
31	SDZ	Shangdianzi, China	117.12	40.65	293	CMA, NOAA/ESRL	continental	Flask: 2009–2013	Y	Y	Y
32	SEY	Mahe Island, Seychelles	55.53	-4.68	7	SBS, NOAA/ESRL	marine	Flask: 2006–2013		Y	Y
33	SNG	Sinhagad, India	73.75	18.35	1600	IITM	mountain	CH_4 flask: 2010–2013 CO_2 flask: 2009–2013	Y	Y	Y
34	SPO	South Pole, USA	-24.80	-89.98	2810	NOAA/ESRL	mountain	Flask: 2006–2013		Y	Y
35	TAP	Tae-ahn Peninsula, Korea	126.13	36.73	21	KCAER, NOAA/ESRL	coastal	Flask: 2006–2013	Y	Y	Y
36	UUM	Ulaan Uul, Mongolia	111.10	44.45	1012	MHRI, NOAA/ESRL	continental	Flask: 2006–2013	Y	Y	Y
37	WIS	Negev Desert, Israel	30.86	34.79	482	WIS, AIES, NOAA/ESRL	continental	Flask: 2006–2013		Y	Y
38	WLG	Mt. Waliguan, China	100.90	36.28	3890	CMA, NOAA/ESRL	mountain	Flask: 2006–2013	Y	Y	Y
39	YON	Yonagunijima, Japan	123.02	24.47	50	JMA	marine	Continuous: 2006–2013	Y	Y	Y

Abbreviations:
Aichi – Aichi Air Environment Division, Japan
AIES – Arava Institute for Environmental Studies, Israel
BMKG – Agency for Meteorology, Climatology and Geophysics, Indonesia
CMA – China Meteorological Administration, China
CSIR4PI – Council of Scientific and Industrial Research Fourth Paradigm Institute, India
CSIRO – Commonwealth Scientific and Industrial Research Organisation, Australia
Empa – Swiss Federal Laboratories for Materials Testing and Research, Switzerland
ESSO/NIOT – Earth System Sciences Organisation/National Institute of Ocean Technology, India
IIA – Indian Institute of Astrophysics, India
IITM – Indian Institute of Tropical Meteorology, India
JMA – Japan Meteorological Agency, Japan
KCAER – Korea Centre for Atmospheric Environment Research, Republic of Korea
KMA – Korea Meteorological Administration, Republic of Korea
KSIEMC – Kazakh Scientific Institute of Environmental Monitoring and Climate, Kazakhstan

LAIBS – Lulin Atmospheric Background Station, Taiwan
LSCE – Laboratoire des Sciences du Climat et de l'Environnement, France
MHRI – Mongolian Hydrometeorological Research Institute, Mongolia
NIER – National Institute of Environmental Research, South Korea
NIES – National Institute for Environmental Studies, Japan
NIWA – National Institute of Water and Atmospheric Research, New Zealand
NOAA/ESRL – National Oceanic and Atmospheric Administration/Earth System Research Laboratory
Saitama – Center for Environmental Science in Saitama
SBS – Seychelles Bureau of Standards, Seychelles
WIS – Weizmann Institute of Science, Israel

Figures

Figure 1 Map of locations of stations within and around the zoomed region. The zoomed grid of the LMDz-INCA model is plotted with the NASA Shuttle Radar Topographic Mission (SRTM) 1km digital elevation data (DEM) as background (http://srtm.csi.cgiar.org). The grey shaded area indicates the region with a horizontal resolution of ~0.66° × ~0.51°. The red close circle (blue cross) represents the atmospheric station where flask (continuous) measurements are available and used in this study.

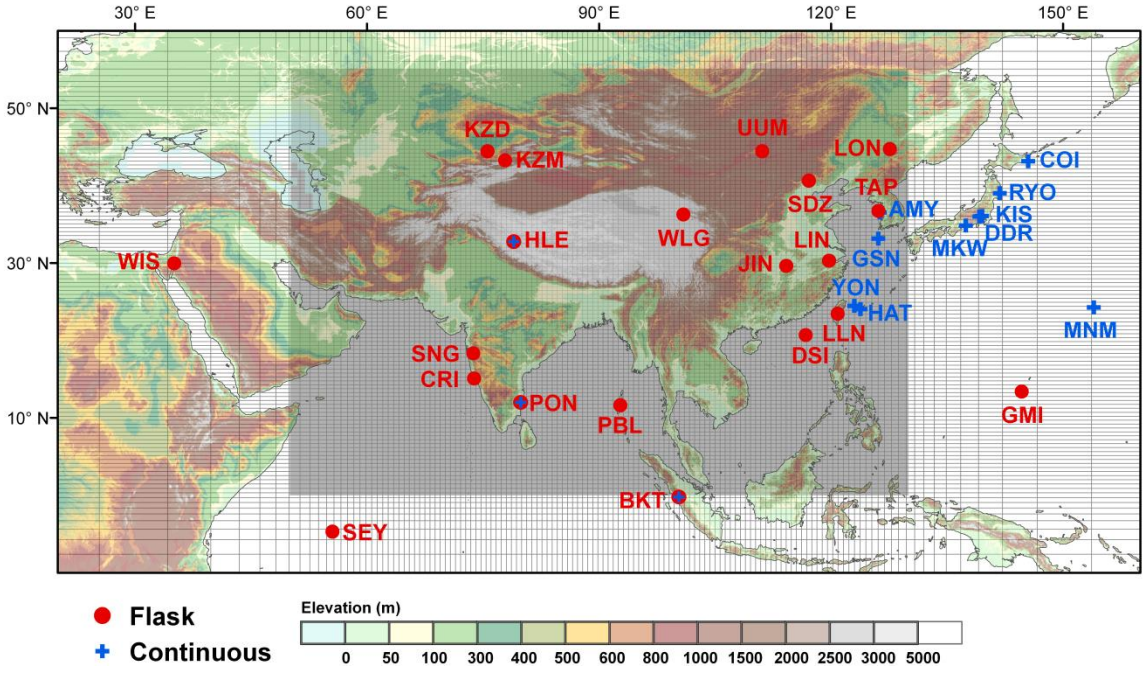

Figure 2 Scatterplots of the simulated and observed mean annual gradients of CH_4 **(a, b)** and CO_2 **(c, d)** between HLE and other stations. In each panel, the simulated CH_4 or CO_2 gradients are based on model outputs from STs (blue circles) and ZAs (red circles), respectively. The black dotted line indicates the identity line, whereas the blue and red dotted lines indicates the corresponding linear fitted lines. The closed and open circles represent stations inside and outside the zoomed region.

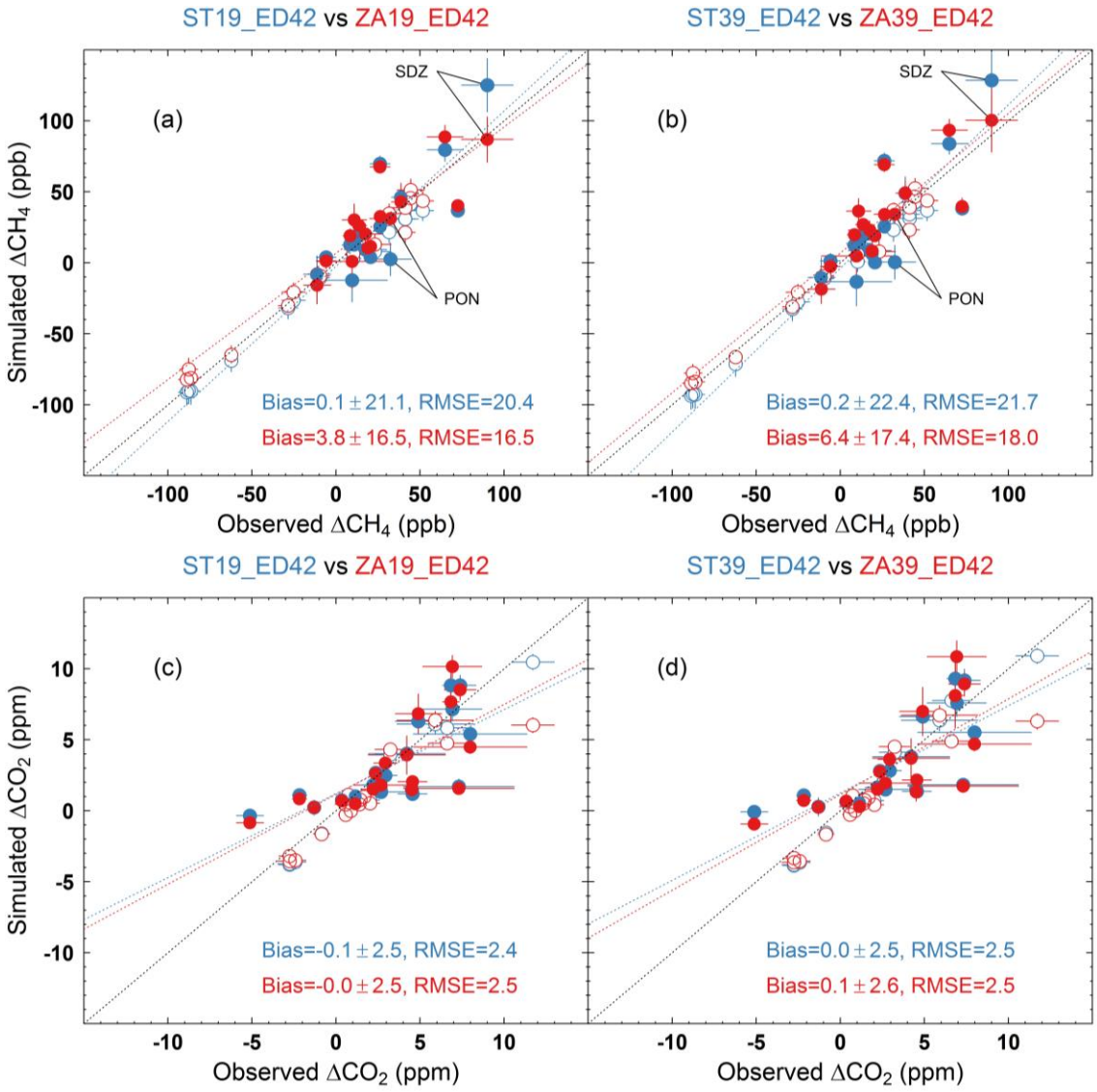

Figure 3 The observed and simulated mean seasonal cycles of CH_4 **(a)** and CO_2 **(b)** for stations within the zoomed region. In each panel, the simulated mean seasonal cycles are based on model outputs from STs (blue lines) and ZAs (red lines), respectively. The text shows statistics between the simulated and observed seasonal cycles for 39-layer models.

(a)

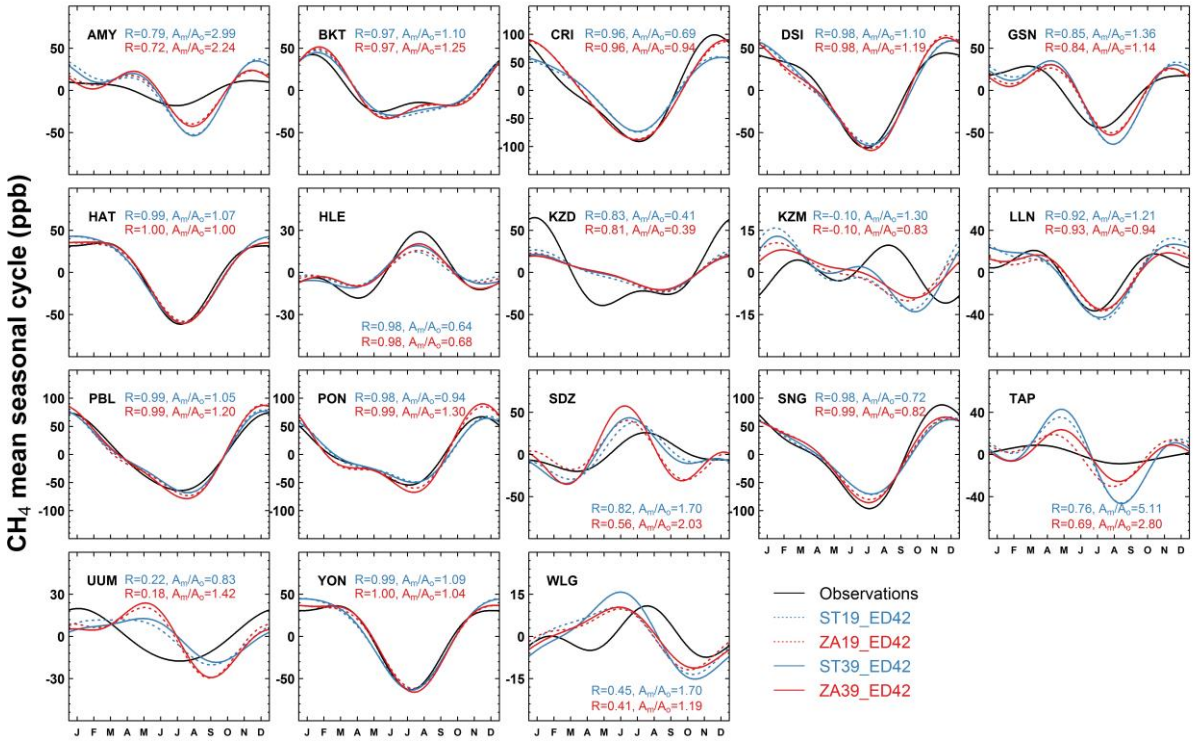

(b)

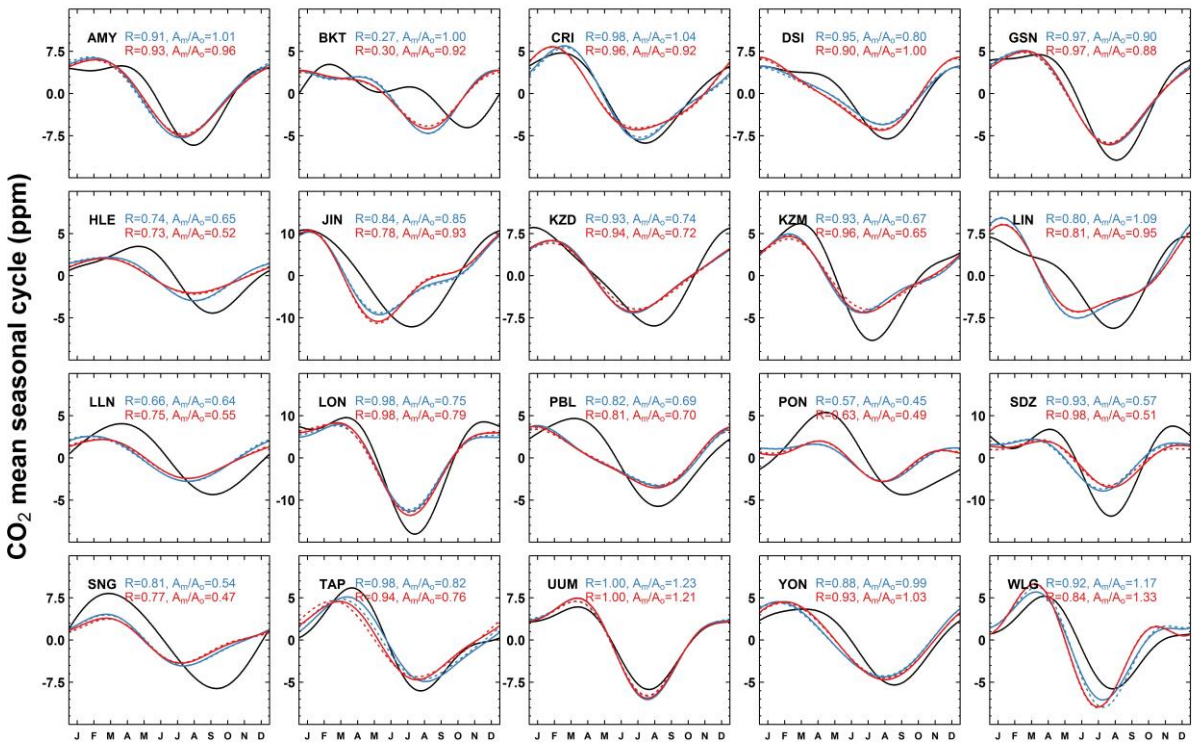

Figure 4 The correlations and normalized standard deviations between the simulated and observed synoptic variability for CH_4 (a,b) and CO_2 (c,d) at stations within the zoomed region. For each station, the synoptic variability is calculated from residuals from the smoothed fitting curve.

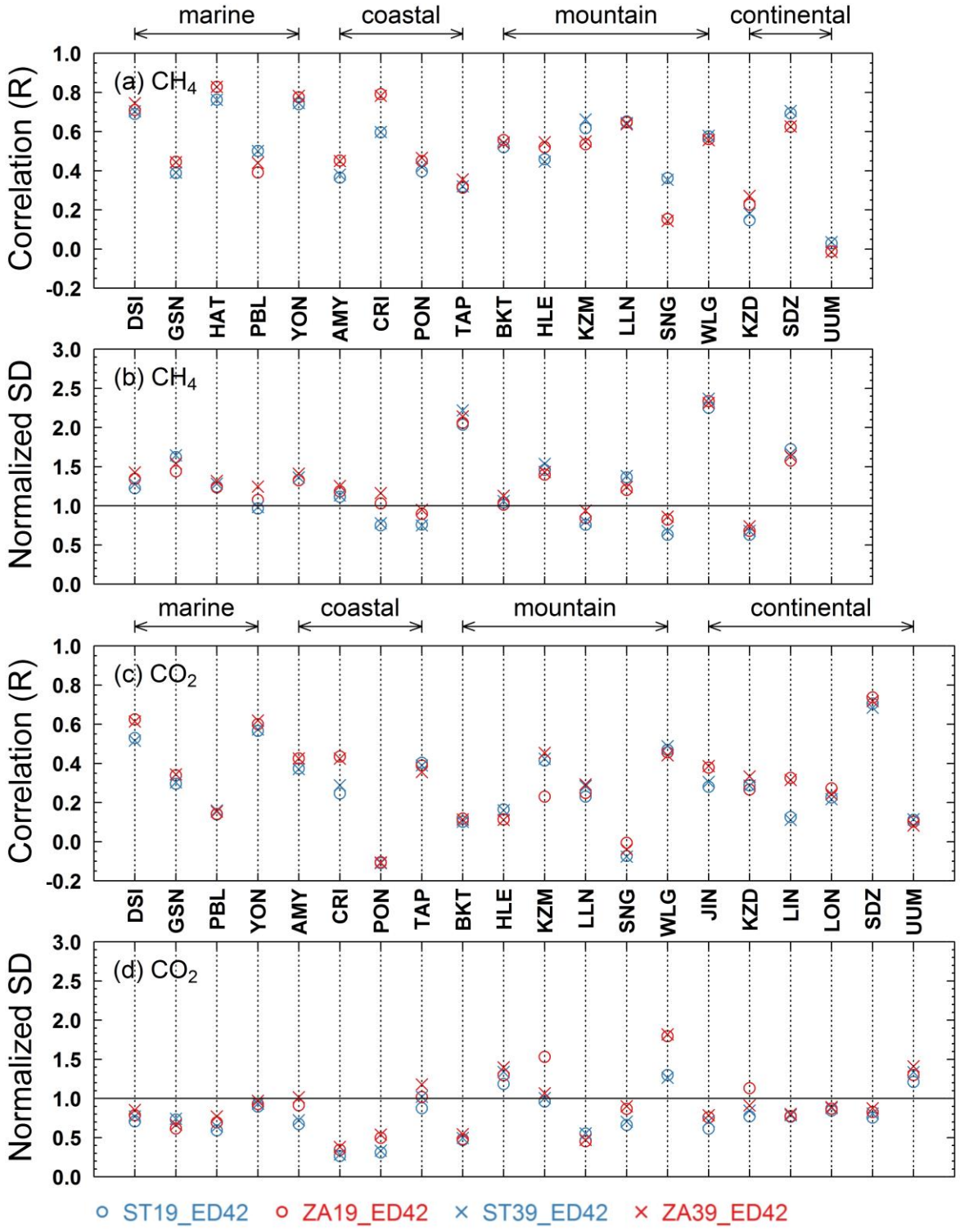

Figure 5 The observed and simulated mean diurnal cycles (in UTC time) of CH_4 **(a)** and CO_2 **(b)** at three stations within the zoomed region. For BKT, the simulated diurnal cycles at lower model levels are also presented.

(a)

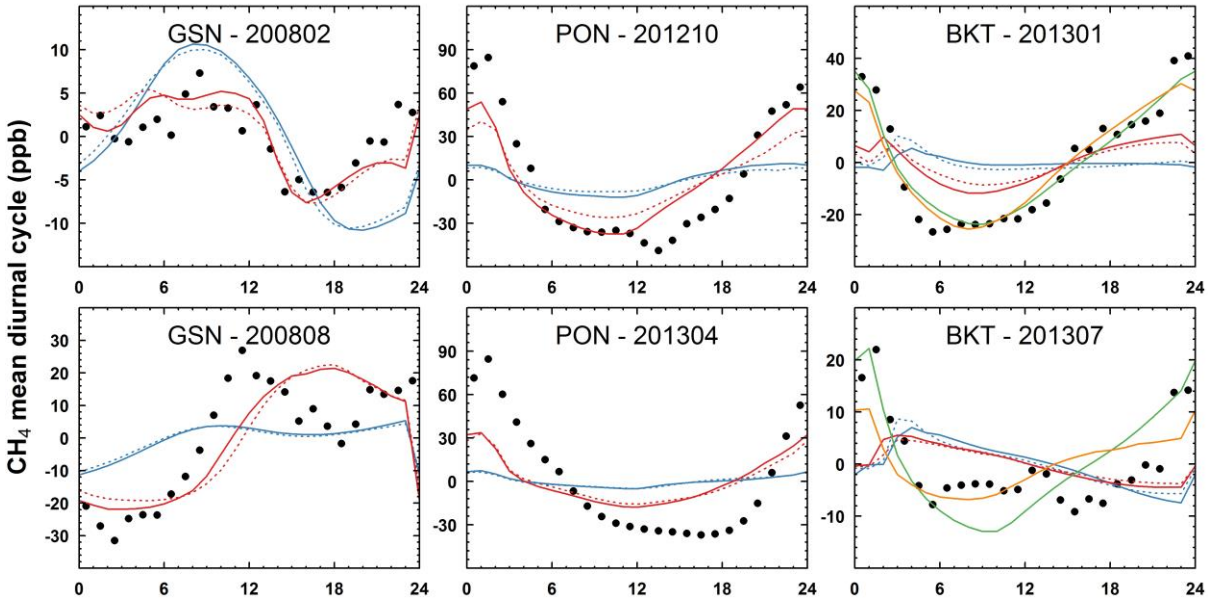

(b)

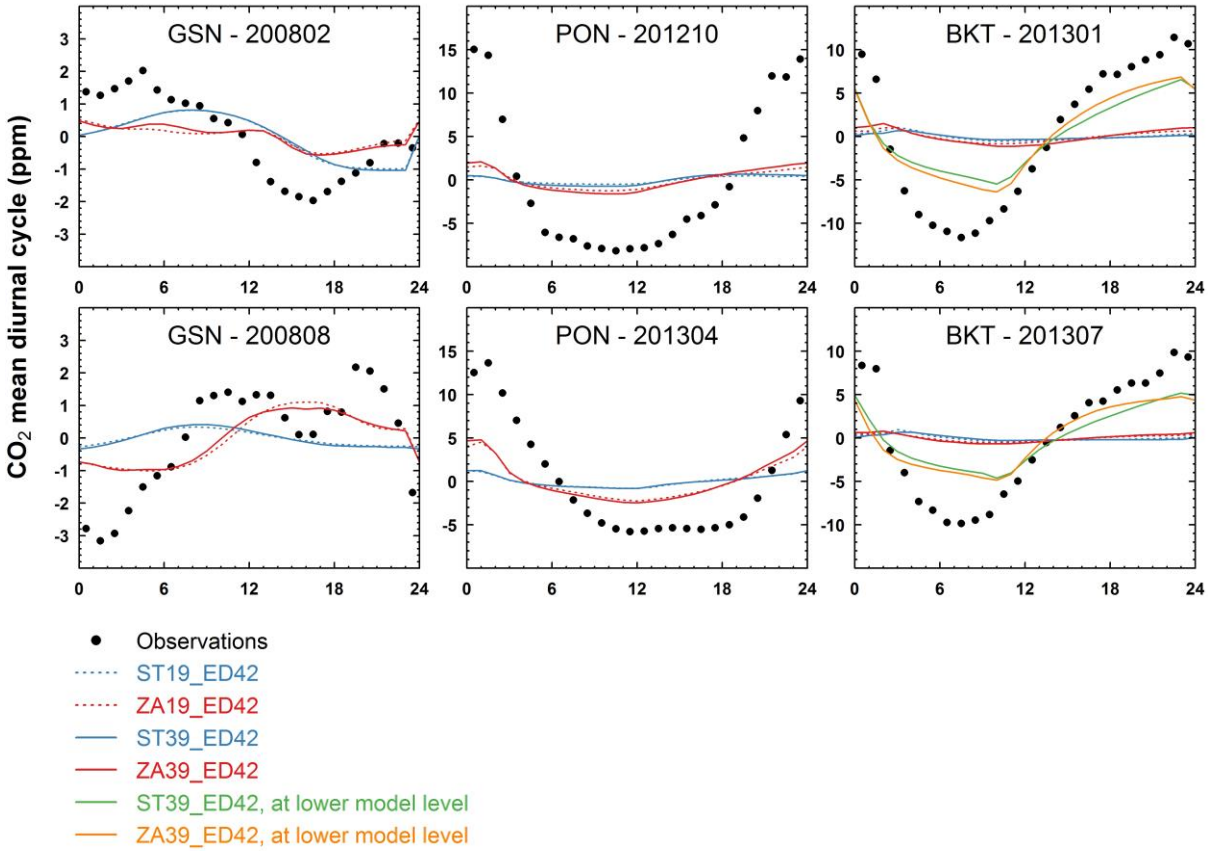

Figure 6 Seasonal mean observed and simulated CO_2 vertical profiles over **(a)** East Asia (EAS), **(b)** the Indian sub-continent (IND), **(c)** Northern Southeast Asia (NSA) and **(d)** Southern Southeast Asia (SSA). The observed vertical profiles are based on CO_2 continuous measurements onboard the commercial air flights from the CONTRAIL project during the period 2006–2011. For each 1-km altitude bin and each subregion, the observed and simulated time series are detrended (denoted as ΔCO_2) and seasonally averaged during January–March (JFM), April–June (AMJ), July–September (JAS) and October–December (OND).

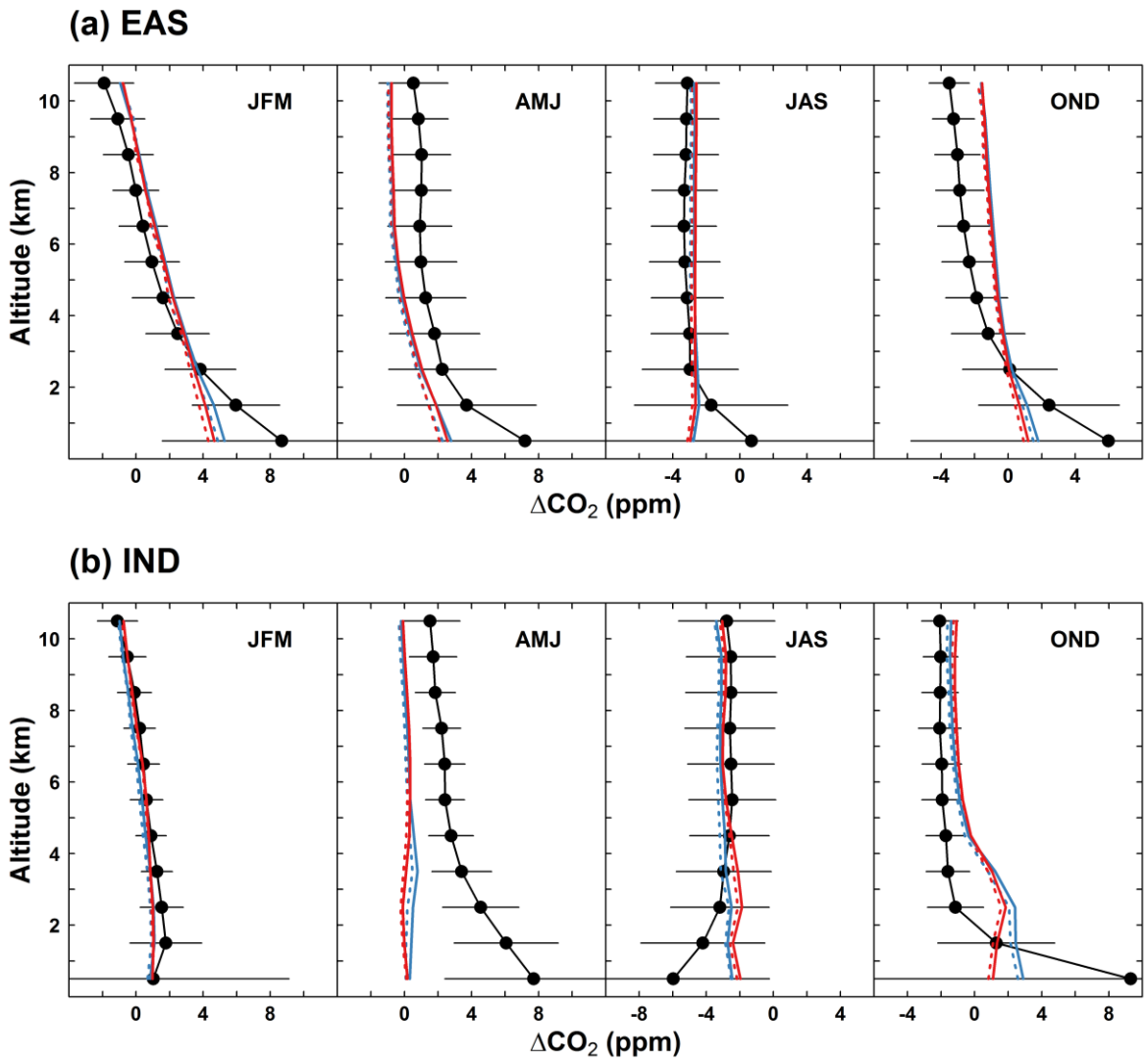

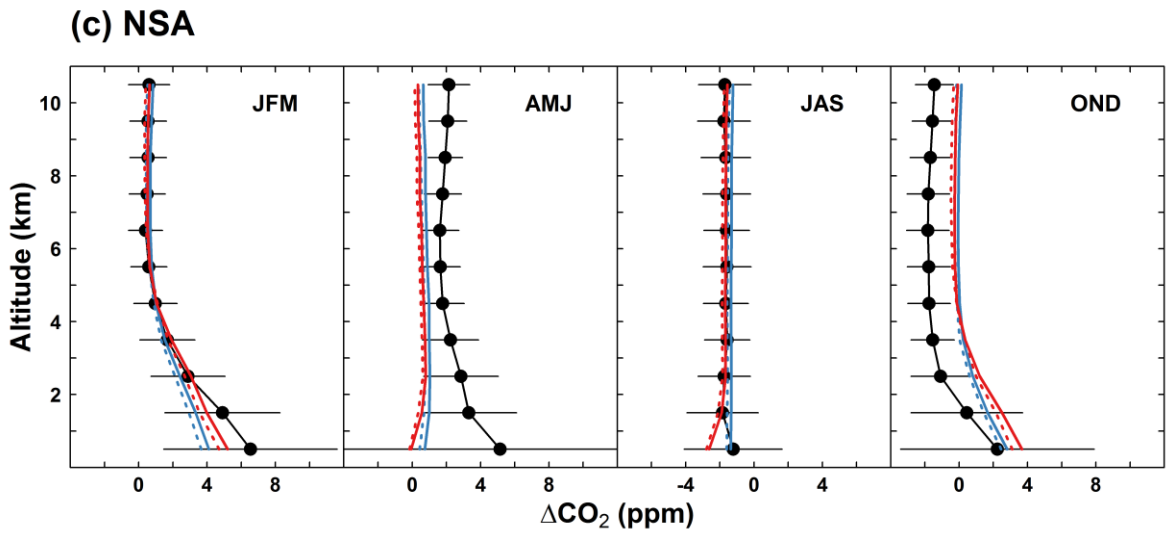

1210

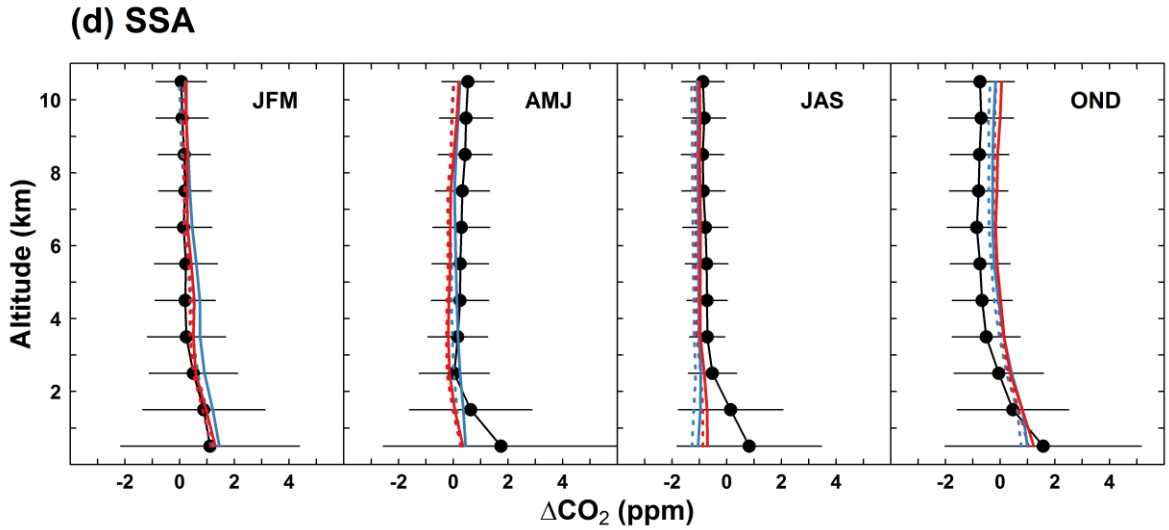

1211
1212

Figure 7 Monthly mean observed and simulated CO_2 gradient between 1 and 4km over **(a)** East Asia (EAS), **(b)** the Indian sub-continent (IND), **(c)** Northern Southeast Asia (NSA) and **(d)** Southern Southeast Asia (SSA). For each subregion, the monthly CO_2 gradients are calculated by averaging over all the vertical profiles the differences in CO_2 concentrations between 1 and 4km.